공학박사 학위논문

Mechanism study of the corrosion and ROS generation on the biodegradable metals for biomedical engineering application

의공학적 응용을 위한 생분해성 금속의 부식 및
활성산소종 생성 메커니즘 연구

2023년 2월

서울대학교 대학원
공과대학 재료공학부

정 고 은

Mechanism study of the corrosion and ROS generation on the biodegradable metals for biomedical engineering application

의공학적 응용을 위한 생분해성 금속의 부식 및 활성산소종 생성 메커니즘 연구

지도교수 장 호 원

이 논문을 공학박사 학위논문으로 제출함
2023년 2월

서울대학교 대학원
공과대학 재료공학부
정 고 은

정고은의 공학박사 학위논문을 인준함
2022년 12월

위 원 장	도 준 상	(인)
부위원장	장 호 원	(인)
위 원	강 승 균	(인)
위 원	김 유 찬	(인)
위 원	옥 명 렬	(인)

Abstract

Magnesium (Mg) is used in various medical engineering fields such as orthopedics, dentistry and etc. due to its excellent mechanical properties, biocompatibility, and biodegradability. Despite these advantages, the use of Mg is limited because of its high corrosion rate. In particular, the dynamic corrosion behavior of the initial corrosion state plays a critical role in cell adhesion and cell-surface bonding and determines the success of implant materials. Therefore, it is very important to understand the corrosion mechanism of Mg. Mg and its alloys generate corrosion products such as hydrogen gas (H2), reactive oxygen species (ROS), and various oxides during the corrosion process. In this dissertation, we aimed to expand their applications in biomedical engineering by understanding the corrosion mechanisms and controlling corrosion products of Mg and its alloys.

Despite innovative advances in stent technology, restenosis is a significant problem for clinical stent implantation. ROS are known to potentially accelerate re-endothelialization and prevent restenosis by selectively controlling endothelial cells (EC) and smooth muscle cells (SMC). In order to generate ROS in the human body, various external stimuli such as ultrasound, light, etc. are required, but galvanic corrosion can easily induce ROS generation with simple coating layers. We report a novel biodegradable hybrid material composed of a biodegradable polymer and double anode/cathode metal layers to enhance re-endothelialization and inhibit restenosis. Pure Zn and Mg thin films were deposited on a poly-l-lactic acid (PLLA) substrate by DC magnetron sputtering, and a long-term immersion test using the biodegradable hybrid material was performed in a phosphate buffer saline (PBS) solution. Both superoxide anions and hydrogen peroxide were produced smoothly even after the positive Mg layer was completely consumed. Therefore, it was concluded that ROS generation by corrosion of PLLA-based hybrid materials could continue until the anode metal layer was depleted.

Second, in biomedical engineering, ROS are recently been actively studied for their excellent potential capability such as antibacterial activity, cancer treatment, etc. However, the corrosion rate of metal was mostly interpreted as the H2 generation. Accordingly, based on metallurgical factors, we tried to find the most prominent factor of ROS generation by the

corrosion of Mg and Mg-based alloys. By measuring the amount of ROS generated by immersing the Mg alloy in the PBS solution, surface properties were applied as more important to ROS generation than electron supply by corrosion. As experimental proof, the surface reaction was thoroughly investigated in an environment where the influence of natural corrosion was minimized by artificially applying a cathode current. As a result, the supply of electrons was not always involved in ROS generation. Another experimental proof, the oxide layer, and ZnO model test, clearly demonstrated that the type of cathode phase, and the oxide layer formed on the surface, that is, the intrinsic characteristics of the alloy surface, are the most important factors in the ROS generation. Through this, based on the microstructure and phase analysis of the surface, it will be possible to predict the dominant reaction of the alloy, and it will be expected that ROS generation can be newly induced through alloy manufacturing, surface coating, and surface treatment.

Third, biodegradable metals have received limited attention for application in transdermal drug delivery, although metallic microneedles (MNs) and iontophoresis have been thoroughly researched for this purpose. Here, we present Mg as a salient candidate for an MN electrode. Its metallic properties enable the application of voltage to enhance the diffusion of charged drug molecules, while H2 generated during Mg corrosion has prevented its application as electrodes. The Mg MN electrode was fabricated using a nanosecond laser, and the amount of H2 was measured during iontophoresis. Accordingly, an appropriate potential window for iontophoresis was established based on the combined effect of enhanced drug diffusion by applied electric potential and impediment from H2. The dye permeation tests of the Mg MN on the porcine skin demonstrated the combined effect of the Mg MN and iontophoresis. The dye migration decreased at higher voltages due to excess H2 and the corrosion of needle tips, both making the diffusion of charged dye molecules along the Mg MN surface harder. These results demonstrate the optimal potential range of Mg MN electrodes for transdermal drug delivery with an electric field and H2 generation during iontophoresis.

As a result, galvanic corrosion, micro galvanic corrosion, and electrochemical corrosion of Mg and Mg-based alloys were analyzed, and the corrosion products were used to confirm their applicability to various biomedical engineering fields such as stent restenosis prevention and

transdermal drug delivery. In the future, based on the above research results, it is expected that the application range of Mg, a biodegradable metal, will be wider, and it will be effectively applied in various fields by appropriately controlling the generation of corrosion products.

Keyword: Magnesium, Magnesium-based alloys, Corrosion, Hydrogen gas, Reactive oxygen species, Biomaterials

Student Number: 2019-31897

List of Figures

Figure 1. Schematic illustration of corrosion mechanism on the surface of the pure Mg.

Figure 2. a) Two metallic bodies form a galvanic corrosion couple and generate ROS-inducing ORR at the cathode surface, b) as a metallic stent body can be the cathode, one anodic layer is necessary for galvanic corrosion, c) as polymeric stents are not conductive, anodic and cathodic double layers are required.

Figure 3. a) Metallic films sputtered on PLLA films, b) SEM images of metal/PLLA hybrid materials, c) XRD spectra of metal on the glass substrate, d) cross-sectional SEM and EDX mapping images of Mg and Zn layer sputtered on the glass substrate (scale bar 2μm).

Figure 4. Line profiles of height, thickness values, and 3D images of a) Zn, b) Mg, and c) Mg/Zn films on the glass substrates analyzed by a confocal laser scanning microscope (LSM; LEXT OLS4100, Olympus, Japan) (Mean ± SD n = 3).

Figure 5. a) Schematic of experimental protocols for long-term immersion test and ROS measurement, b) superoxide anion generation behavior of Mg/PLLA and Mg/Zn/PLLA hybrid materials for 14 days, c) hydrogen peroxide generation behavior of Mg/PLLA and Mg/Zn/PLLA hybrid materials for 14 days. (Mean ± SD n = 4)

Figure 6. The measurement of hydrogen gas generation amount on the MP and MZP hybrid materials for 1 h on day 0.

Figure 7. Schematic illustration of ROS generation/conversion reactions and their potential levels together with oxidation of Mg and Zn. (ROS generation and conversion reactions and their potential values)

Figure 8. Schematic image of stent inserted blood vessel. After the stent was inserted, because the cell layers are soft enough, the stent tightly fits into the inner vessel wall, then the layers of endothelial cells and smooth muscle cells surround the stent.

Figure 9. Measurement of the pH variance a) around MZP hybrid materials depending on the system size, and b) around MP and MZP hybrid materials during the immersion test for 1 h on day 0.

Figure 10. Schematic illustration of micro galvanic corrosion mechanism on the surface of the

Mg-based alloy.

Figure 11. (a) SEM images of i) CZ50, ii) CZ51, iii) pM, iv) Z3M, and v) Z3S, (b) XRD spectra of bare specimens. (scale bar: 20μm)

Figure 12. The amount of a) H_2 generated and b) ROS generation of the five specimens in PBS solution for 1 h. Schematic illustration of the cathodic reaction on the c) CZ50 and d) Z3M surface during the immersion test.

Figure 13. a) Schematic illustration of the corrosion of the pure Mg under a cathodic current, b) the potential difference under a cathodic current of the five specimens in PBS solution for 1 h, c) the amount of ROS generation of the five specimens under a cathodic current in PBS solution for 1 h.

Figure 14. a) Schematic illustration of the surface reaction in CZ50 under a cathodic current, b) the Mg ions releasing amount in PBS solution during immersion test and cathodic current test by ICP-OES, c) the O/Mg atomic ratio after immersion test and cathodic current test by EDS analysis

Figure 15. a) Schematic illustration of the surface reaction in Z3M under a cathodic current, b) schematic graph of the potential values of H_2/ROS generation reactions and of each phase in CZ50 and Z3M, c) schematic graph of the band gap of ZnO and $Mg(OH)_2$ as the representative oxide layers.

Figure 16. TEM images of a) the cross-section EDS analysis, and b) the thickness of the oxide layer on the corroded Z3M surface in i) immersion test and ii) cathodic current test.

Figure 17. a) XPS survey spectrum of the corroded Z3M surface, b) high-resolution deconvoluted XPS spectra for Zn 2P on the corroded Z3M surface in i) immersion test and ii) cathodic current test, c) XRD pattern of the bare and corroded Z3M specimens, d) TEM images and experimental SAEDs collected on the oxide layer of the corroded Z3M in i) immersion test and ii) cathodic current test.

Figure 18. a) Schematic illustration of oxide layer model test, b) the amount of ROS generation in oxide layer model test under a cathodic current in PBS solution for 1 h, c) the process by ImageJ software to measure the area fraction of Zn-rich regions on Z3M specimen, d) cross-section SEM image of ZnO layer sputtered on pM specimen, sample images of e) 30%

ZnO_30min and f) 30% ZnO_1min i) before and ii) after ZnO model test, g) the amount of ROS generation in ZnO model test under a cathodic current in PBS solution for 1 h.

Figure 19. Schematic illustration of the iontophoretic Mg microneedle electrodes for diffusion of drug molecules into the skin.

Figure 20. a) The fabrication process of the Mg microneedles, b) optical images of the 6 x 2 array of Mg microneedles, c) visualization of microchannel created by the Mg microneedles with Rhodamine B into the porcine samples (scale bar: 2 mm), d) close up image (scale bar: 200 μm), e) 3D depth microscopy profile image (scale bar: 200 μm) and f) the average depth of a single puncture on the porcine sample stained by Rhodamine B after 1 hour of the Mg microneedle insertion. (Mean ± SD, n = 10)

Figure 21. Fundamental study of Mg electrodes a) the potential of each pure Mg electrode under the applied potential (vs. Ag/AgCl), b) H_2 generation and c) H_2 generation rate curves of the pure Mg electrodes under the applied potential, d) the potential window of the pure Mg electrodes based on the amount of H_2 generation at fixed times, f) the potential and g) H_2 generation curve of Mg-0.05Ca-1Zn electrodes under the applied potential (vs. Ag/AgCl), h) the potential window change of the Mg based metals based on the amount of H_2 generation at 1 h.

Figure 22 a) Schematic illustration of experimental set up of the dye migration test during iontophoretic investigations, b) optical cross-sections images of the porcine samples after 1 h of insertion under the applied potential (scale bar: 1mm), c) current change curve for 1 h of Mg microneedle insertion into the porcine skin under the applied potential.

Figure 23. a) The area analysis process of dye migration in the porcine samples after 1 hour of Mg microneedle insertion under the applied potential. b) area change curve of dye migration after 1 hour of insertion under the applied potential. (One-way ANOVA with Turkey's test Mean ± SD n = 5, n.s = no significant *p<0.05, **p<0.01, ***p<0.001, ****p<0.0001)

Figure 24 a) SEM images of i) the Mg microneedle anode and ii) the Mg microneedle cathode after 1 h of insertion into the porcine sample under 0.8 V (scale bar: 100 μm), b) SEM images of the Mg microneedle anodes after 1 h of insertion into the porcine samples under the applied potential (scale bar: 100 μm), c) H_2 generation curve on each pure Mg electrode under the applied potential for 1 h, d) schematic illustration of the H_2 and H_2O_2 generation mechanism on

each pure Mg electrode, e) total H_2O_2 generation on the pure Mg electrodes under the applied potential for 1 h.

List of Tables

Table 1. Analysis of the Mg and Zn ion releasing amount in the PBS solution during immersion testing for 1 h on day 0 by ICP-OES.

Table 2. The EDS atomic percentage of each phase on the bare specimens.

Table 3. Elemental composition by EDS of a) the Mg microneedle (MN) electrodes after 1 h of insertion into the porcine sample at 0.8 V, and b) the Mg MN anodes after 1 h of insertion into the porcine samples under the applied potential.

Contents

Abstract……. i

List of Figures……. iv

List of Tables……..... viii

Contents ……..... ix

Chapter 1. Introduction 1

1.1 Study Background 1

1.1.1 Mg and Mg-based alloys as biomaterials..... 1

1.1.2 Biodegradable corrosion of the Mg and Mg-based alloys 2

1.1.3 Corrosion products by corrosion of the Mg-based materials 5

1.2 Objective of this study..... 6

Chapter 2. Development of Organic/Inorganic Hybrid Materials for Fully Degradable Reactive Oxygen Species-Releasing Stents for Anti-restenosis 7

2.1 Introduction 7

2.2 Experimental Procedures..... 10

2.2.1 Sample preparation 10

2.2.2 Material characterization 10

2.2.3 Long term immersion test 11

2.2.4 Spectroscopy measurements 11

2.3 Results and Discussion..... 13

2.3.1 Biodegradable hybrid materials 13

2.3.2 Long term immersion test 16

2.4 Conclusion..... 24

Chapter 3. ROS generation behaviors by various Mg-based alloys 25

3.1 Introduction 25

3.2 Experimental Procedures..... 28

3.2.1 Specimen preparation 28
3.2.2 ROS measurement 28
3.2.3 H_2 measurement 29
3.2.4 Electrochemical test 29
3.2.5 Characterization 29
3.2.6 Oxide layer and ZnO model test 30
3.3 Results and Discussion 31
3.3.1 Mg-based alloys 31
3.3.2 Immersion test 33
3.3.3 Cathodic current test 36
3.3.4 Surface analysis of corroded Z3M 43
3.3.5 Oxide layer and ZnO model test 46
3.4 Conclusion 49

Chapter 4. Biodegradable Mg Electrodes for Iontophoretic Transdermal Drug Delivery. 50
4.1 Introduction 50
4.2 Experimental Procedures 53
4.2.1 Fabrication of the Mg MN 53
4.2.2 Penetration test of the Mg MN 53
4.2.3 Potential measurement of the Mg and Mg alloys electrodes 53
4.2.4 H_2 generation test of the Mg and Mg alloys electrodes 54
4.2.5 H_2O_2 generation test of the Mg electrodes 54
4.2.6 Dye permeation test on the porcine skin 55
4.2.7 Area analysis for dye migration 55
4.2.8 Mg MN Characterization 55
4.3 Results and Discussion 56
4.3.1 Fabrication and penetration test of the Mg MN 56
4.3.2 Establishment of applied potential range 58
4.3.3 Dye permeation test on the porcine skin 61

4.3.4 Characterization of the Mg MN electrodes 65

4.3 Conclusion 67

Chapter 5. Conclusion 68

References 70

국문초록 87

Chapter 1. Introduction

1.1 Study background

1.1.1 Mg and Mg-based alloys as biomaterials

Biomaterials, which are the basic materials of artificial tissues and organs, collectively refer to materials that are in direct contact with living tissues as a means of diagnosis, treatment, and prevention of diseases [1]. In particular, it is used to replace morphological and functional defects of damaged or dysfunctional human tissues and organs [2]. In practice, polymer, metal, and ceramic materials are used, and the application range is very diverse. Representative properties required as biomaterials are biofunctionality and biocompatibility [3]. Biofunctional properties such as chemical stability, adequate mechanical strength, appropriate design, and easy processability are required to fully perform the target function while the biomaterial exists in the body. In addition, when a biomaterial comes into contact with a living tissue or body fluid, it should not exhibit a rejection reaction, and the interaction with the living tissue should be smooth.

Because metal materials are excellent in strength, toughness, and rigidity, they are used in orthopedics for fracture fixation, artificial joints, etc [2-3]. It is desirable that these devices be quickly removed when their duties have been completed, but reoperation is required and the patient is inevitably burdened. In order to avoid such a burden, a biodegradable metal material that is gradually decomposed and lost in the body is attracting attention.

Magnesium (Mg), one of the representative biodegradable metals, is an essential element that occupies a large amount of the fourth mineral constituting the human body. In addition, it is a metal element with excellent biocompatibility enough to form calcium phosphate, a substance similar to bone, by reacting with calcium ions in body fluids and phosphoric acid [4]. It has been reported that the density of Mg is 1.74 - 2.0 g.cm^3, which is similar to that of hard tissue (1.8 - 2.1 g/cm^3) in humans and lower than that of Ti (4.4 - 4.5 g/cm^3) [4-5]. The fracture toughness of Mg is higher than that of ceramic. With an elastic modulus similar to that of bone, Mg-based alloys prevent the stress-shield effect. For its excellent biocompatibility and mechanical properties similar to those of human bone, Mg has been considered as a potential

candidate for applications in orthopedics, dentistry, etc [6]. Above all, the biodegradable properties of Mg are very noteworthy [7]. When implants are inserted into the human body, biodegradable metallic materials heal fractures, replace broken bones, and self-degrade. The advantage of using a biodegradable metal material for implantation is that no secondary surgery is required after implantation [8].

When using Mg, its alloys whose performance has been improved to suit the purpose are often used rather than the pure metal [9-11]. As a representative biodegradable metal, the Mg-based alloys have already been actively studied in various fields such as orthopedics [12-13], dental [14], and cardiology [15]. These properties have been improved by an advanced casting process and the design of alloying-added elements [9-11]. Additional elements for reinforcing the mechanical properties of mg alloys should be nontoxic. Typical alloying elements in Mg-based alloys are calcium (Ca), zinc (Zn), manganese (Mn), and zirconium (Zr), which are present in the human body [16-17]. The Ca element is a major component in human bone, furthermore, it is involved in human metabolism and chemical signaling with cells [17]. It has been evaluated that the addition of Zn, Mn, and Zr enhanced mechanical and corrosion properties by changing microstructure such as grain sizes and phases [18-20].

1.1.2 Biodegradable corrosion of the pure Mg metal

Despite these advantages, the most limiting reason for the use of Mg is its aggressive corrosion rate. Mg corrosion proceeds through the following chemical reactions [21];

$Mg \rightarrow Mg^{2+} + e^{-}$ (anodic reaction)

$2H_2O + 2e^{-} \rightarrow H_2 + 2OH^{-}$ (cathodic reaction, water decomposition reaction)

$O_2 + e^{-} \rightarrow \cdot O_2^{-}$ (cathodic reaction, oxygen reduction reaction)

$\cdot O_2^{-} + 2H^{+} + 2e^{-} \rightarrow H_2O_2$

Electrons generated as metals corrode participate in chemical cathodic reactions such as water decomposition and oxygen reduction reactions (ORR) (**Figure 1**) [22-23]. The water decomposition reaction generates hydrogen gas (H_2) and OH^{-} to raise the surrounding pH and alkalinize it. On the other hand, in ORR, dissolved oxygen in the solution meets electrons on the surface to generate the reactive oxygen species (ROS); superoxide anion ($\cdot O_2^{-}$), and hydrogen

peroxide (H_2O_2) in turn [24-25]. In particular, the dynamic corrosion process in the initial corrosion stage plays a decisive role in cell attachment and surface-cell bonding and determines the success of implant materials [26-28]. Therefore, it is very important to understand the corrosion mechanism of Mg and Mg-based alloys.

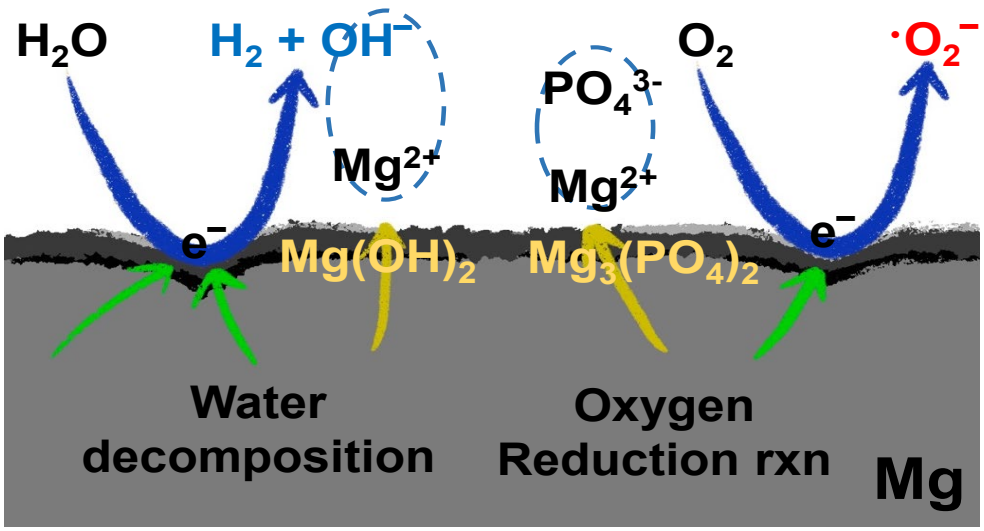

Figure 1. Schematic illustration of corrosion mechanism on the surface of the pure Mg.

1.1.3 Corrosion products by corrosion of the Mg-based materials

Mg and Mg-based alloys generate corrosion products such as H_2, ROS, and various oxides during the corrosion process. The electrons participating in water decomposition generate H_2, and it has been studied in a positive or negative way in the use of Mg-based alloys. Hydrogen pockets generated by active corrosion of Mg metal during implant insertion [29-30] led to the development of alloys with high corrosion resistance to control the corrosion rate by applying the methods such as Mg-based alloys, surface coating, surface treatment and etc [11, 31-32]. On the other hand, the high reactivity of Mg is attracting attention as it can deliver drugs farther from the microneedle during transdermal drug delivery [33], as well as increase the therapeutic effect by increasing the pH of the surrounding environment during cancer treatment [34].

In most studies dealing with the corrosion rate of the Mg, only this amount of H_2 generated is explained and analyzed. However, electrons generated as the Mg corrodes can also react with dissolved oxygen in the solution to generate ROS [35-36]. Mg corrosion is actively involved in ROS generation as a very promising antibacterial agent [37-41]. ROS are actively studied in the field of biomedical engineering by treating cancer and killing harmful bacteria with their excellent antibacterial activity [42-44]. In addition, they are recently in the spotlight in the fields of catalyst and environment as well [45-46]. For this reason, it has become important to understand the tendency of ROS generation due to Mg corrosion. As such, the products produced by the corrosion reaction of Mg based alloys are widely applied in the field of biomedical engineering.

1.2 Objective of this study

This dissertation aims to expand the possibilities to various biomedical engineering applications by understanding the corrosion mechanism of Mg and Mg-based alloys and controlling the amount of corrosion products generated. Mg-based materials are used in various medical engineering fields such as orthopedics and dentistry due to its excellent mechanical properties, biocompatibility, and biodegradable properties. This thesis consists of three parts.

First, we tried to prevent re-endothelialization during stent insertion by inducing galvanic corrosion and promoting ROS using a coating layer of biodegradable metals Mg and Zn. In order to generate ROS on the metal oxides in the human body, various external stimuli such as ultrasound and light are required, but galvanic corrosion can easily induce ROS generation with a simple coating layer.

Second, the ROS generation mechanism of Mg and Mg-based alloys was studied. The corrosion rate of these metals was mostly interpreted as the evolution of H_2. However, as the importance of antibacterial activity and cancer treatment by ROS has emerged in the field of medical engineering, we have sought to expand the use of Mg-based alloys in various fields by identifying the main factors that generate ROS on metal surfaces.

Third, we tried to apply it to the field of safe and efficient transdermal drug delivery by controlling drug delivery through electrochemical corrosion of Mg. The active corrosion rate of Mg has made its use as an electrode difficult. However, its excellent biocompatibility properties make it a very attractive biodegradable microneedle candidate by combining with iontophoresis.

Chapter 2. Development of Organic/Inorganic Hybrid Materials for Fully Degradable Reactive Oxygen Species releasing stents for anti-restenosis

2.1 Introduction

Despite innovative advances in stent technologies, in-stent restenosis (ISR) remains a crucial issue for the clinical implantation of stents [47-48]. The early success of bare metal stents (BMSs) was overshadowed by the high ISR ratio (17–41% [47]), and drug-eluting stents (DESs) have been introduced to suppress neointima growth and proliferation of smooth muscle cells [49-50]. Due to the importance of preventing ISR problems, not only the drug-eluting stents, but also some other multifunctional stent studies such as metal coating, or polarizing surface of the clinical stents are being conducted in the biomedical fields [51-53]. However, the remaining metallic stent material can stimulate endothelial cell layers, resulting in endothelial dysfunction, disruption of blood flow with thick struts, and an increase in the risk of blood clot formation [54-57]. Therefore, current trends in stent R&D involve the development of "biodegradable stents" using biodegradable metals (Mg, Fe, Zn) or polymers so that if ISR occurs, additional stent implantation can be performed [58-59]. Recently, Park and Seo proposed a ROS-generating galvanic system consisting of a biodegradable Mg film (anode) and NiTi base metal (cathode) for stent application (as described in **Figure 2a** and **2b**), based on the biochemical functions of ROS: selectively controlling endothelial cells (EC) and smooth muscle cells (SMC), and potentially accelerating re-endothelialization and lowering the risk of ISR [60]. As biodegradable polymers are not electrically conductive, double metallic layers are required to constitute a galvanic couple for ROS generation, as shown in **Figure 2c**.

In the biomedical field, ROS is produced by exciting electrons to the conduction band by applying external stimuli such as ultrasound or light to metal oxides [61-62]. However, galvanic corrosion can generate ROS by the simple potential differences between two metals without external stimuli in an electrolyte solution. It induces ROS generation by accelerating the corrosion of anodic metal inside and generating more electrons than in a single metal [63-65].

Here, we report new biodegradable hybrid materials composed of a biodegradable polymer substrate and double anodic/cathodic metallic layers for potential application in biodegradable stents that enhance re-endothelialization and suppress restenosis. Pure Zn and Mg films (approximately 3-μm thick) were deposited onto PLLA substrates to form a galvanic corrosion couple, and a long-term immersion test using the biodegradable hybrid materials was performed in PBS for 2 weeks. The concentrations of superoxide anions ($\cdot O_2^-$) and hydrogen peroxide (H_2O_2) generated by the corrosion of biodegradable metallic films were monitored every one or two days. To resolve the safety issues associated with the stent application, the corrosion products of the metal films in PBS were analyzed.

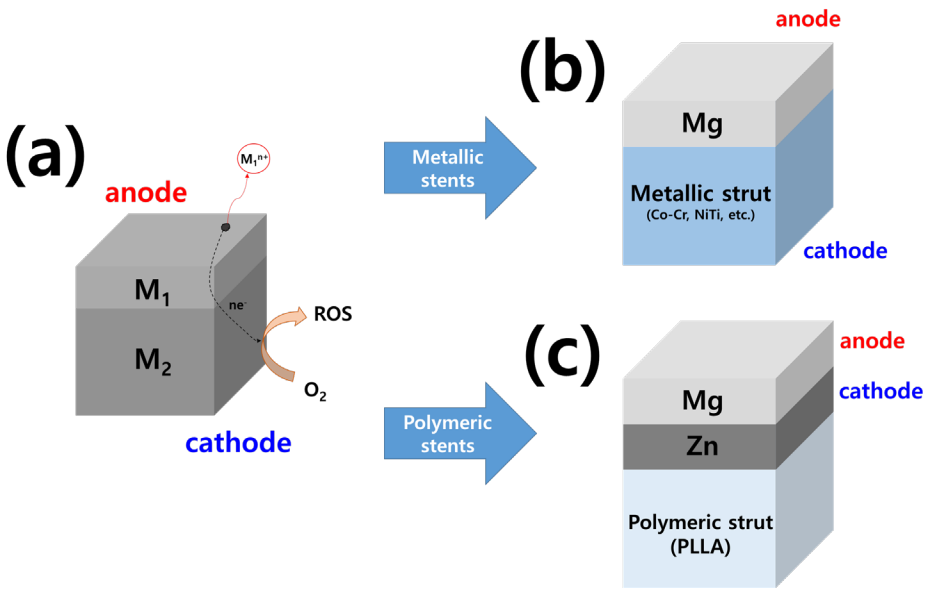

Figure 2. a) Two metallic bodies form a galvanic corrosion couple and generate ROS-inducing ORR at the cathode surface, b) as a metallic stent body can be the cathode, one anodic layer is necessary for galvanic corrosion, c) as polymeric stents are not conductive, anodic and cathodic double layers are required.

2.2 Experimental procedures

2.2.1 Sample preparation

Medical-grade biodegradable poly-l-lactic acid (PLLA) extruded ribbons (25.4 mm × 12.7 mm, t = 127 ± 30 μm) were purchased from Zeus Inc. (Orangeburg, SC, USA). A DC magnetron sputtering machine (Korea VAC-TEC Co. Ltd., Republic of Korea) equipped with pure Zn (4N, VTM Co, Republic of Korea) and pure Mg (4N, iTASCO, Republic of Korea) sputter targets was used for the deposition of the metallic layers. Medical-grade PLLA films were cut to 16 mm × 10 mm, and three types of biodegradable hybrid materials were prepared: Mg on PLLA (MP), Zn on PLLA (ZP), and Mg/Zn on PLLA (MZP). The area of the metallic films was 1 cm^2. The base and process pressures were 4.0×10^{-5} Pa and 0.40 Pa, respectively. The Ar flow rate was 10 standard cubic centimeters per minute (SCCM). The deposition rate of Mg was approximately 0.036 μm/min, with a sputtering power of 130 W, and that of Zn was approximately 0.042 μm/min, with a sputtering power of 100 W.

2.2.2 Material characterization

Field-emission scanning electron microscopy (FE-SEM; Inspect F50, FEI) was used to observe the morphology of the deposited metallic film surfaces and their corrosion products. The elemental compositions of the corroded film surfaces were observed using energy-dispersive X-ray spectroscopy (EDX; Inspect F50, FEI). Both the FE-SEM and EDX measurements were performed at an accelerating voltage of 10 kV. The phases of the metallic layers were analyzed by X-ray diffraction (XRD) using a diffractometer (D8 Advance, Bruker, Germany) with Cu Kα radiation (λ = 1.5406 Å) operated at 40 kV and 40 mA. The scanning range was 10 – 90° in 2θ with a step size of 0.01° (50 s per step). The line profiles of the height and the 3D images of the samples were analyzed using a confocal laser scanning microscope (LSM; LEXT OLS4100, Olympus, Japan). A 20 × lens was used in non-contact mode. Average values were evaluated at three points on the surface of each sample. Glass substrates were used instead of PLLA for XRD, cross-sectional SEM, and line profiles measurements as the effect of substrates for those measurements was negligible and both materials had amorphous

morphologies.

2.2.3 Long term immersion test

Immersion tests were carried out to measure the change in the ROS generation rate over the long term and to observe the corrosion behavior of the metallic films. The metallic samples were soaked in 1× phosphate buffered solution (PBS, pH 7.4, Welgene) containing NaCl, KCl, Na_2HPO_4, and KH_2PO_4, and stored at 37 °C in a water bath after being wrapped in parafilm to prevent evaporation. Half of the PBS solution was replaced every day at a fixed time to simulate human diuresis [66]. The ROS detection of the samples was also investigated at a fixed time and temperature. Each sample was immersed in a new PBS solution and the ROS generation ability was measured for 1 h. Samples were replaced in the original PBS solution and stored at 37 °C in a water bath. In particular, the amount of hydrogen gas generation, pH variance, and the releasing amount of Mg and Zn ions in the PBS solution were investigated for detailed analysis of galvanic corrosion and ROS generation of hybrid materials during the immersion for 1 h on day 0. The MP and MZP hybrid materials were immersed in PBS solution and the volume change according to the H_2 generation was observed at the column of the inverted funnel. The pH variance around the MP and MZP hybrid materials was measured using a pH meter (Lab 850, SI Analytics®, Germany). Then, the inductively coupled plasma optical emission spectroscopy (iCAP 6000 Series, Thermo, US) was conducted at 166 ~ 847 nm of wavelength range under argon gas for analysis of Mg and Zn ion releasing amount in the PBS solution during the immersion.

2.2.4 Spectroscopy measurements

The dye products from the $\cdot O_2^-$ and H_2O_2 were measured using a GloMax® Discover Microplate Reader (Promega, USA). The XTT (2,3-bis-(2-methoxy-4-nitro-5-sulfophenyl)-2H-tetrazolium-5-carboxanilide) cell proliferation kit (Abcam, UK) was used to detect $\cdot O_2^-$. When the tetrazolium salt meets the superoxide anion, the salt turns into XTT formazan dye, and the absorbance is detectable at the 450-nm wavelength. After immersion of the samples in the XTT solution for specific durations, a sampling solution was prepared, and the absorbance of each

sample was measured. There is no standard solution for $\cdot O_2^-$ owing to their instability, so the obtained qualitative absorbance values were converted to quantitative concentrations using the Beer–Lambert law [67]. The Beer–Lambert law is defined as $A = \varepsilon c \ell$, where A is the value of the absorbance of the material; ε is the molar attenuation coefficient of the material; c is the molar concentration of the species; and ℓ is the path length in centimeters that the light passes through. Here, A can be measured with the instrument, ε refers to the value of the XTT reagent in the reference literature (21.6 mM^{-1} cm^{-1}) [68], and ℓ can be calculated from the volume (100 μl) used in the 96 microplate. Therefore, the quantitative concentration of $\cdot O_2^-$ can be calculated from the equation; $c_{superoxide\ anion} = \frac{A}{21.6 \times 0.303} (mM)$, according to the Beer–Lambert law.

A fluorometric H_2O_2 assay kit (Sigma, USA) was used to measure H_2O_2 generation. After immersing the samples in PBS, the solution was collected at each time point and mixed with the H_2O_2 assay reagent. Twenty minutes after mixing, the intensity of the fluorescence product (resofurin) was measured at λ_{ex} = 540 nm and λ_{em} = 590 nm. The fluorescence intensity was calculated from a standard curve of the known concentration of H_2O_2.

2.3 Results and Discussion

2.3.1 Biodegradable hybrid materials

Biodegradable hybrid materials composed of biodegradable polymer substrate (PLLA) and double anodic/cathodic metallic layers (Mg/Zn), designated as "MZP," were fabricated to evaluate their long-term ROS generation behavior. Additionally, hybrid materials with a single metallic layer and PLLA (Mg/PLLA designated as "MP" and Zn/PLLA as "ZP") were prepared to study the intrinsic corrosion and ROS generation properties of Mg and Zn metallic films. In **Figure 3a**, images of the ZP, MP, and MZP hybrid materials are shown. The ZP sample had a dark gray color with no gloss, whereas the MP sample had a shiny light gray color. The MZP had a light-gray surface with mild gloss. The surface morphology of the hybrid materials in **Figure 3b** shows that the ZP had a rough surface composed of Zn grains around 1 μm in size, whereas the MP consisted of hexagonal Mg flakes densely packed almost parallel to the surface and relatively flat, as confirmed by the strong (002) peak in **Figure 3c**. The surface of the MZP was also rough, consisting of flower-like modules larger than 2 μm in size and coarser than the Zn grains on the ZP surface. The Mg anode layer, approximately 3-μm thick, was deposited onto the cathode Zn film, showing a rough surface morphology with large grains around 1 μm in size. The surface of the Mg film on the Zn layer was composed of flower-like modules larger than the Zn grains, as shown in **Figure 3b**. The XRD patterns of the MZP sample in **Figure 3c** were consistent with the phase content showing a relatively similar intensity of Mg peaks but a weaker intensity of Zn peaks compared to that of single Mg and Zn. In **Figure 3d**, the cross-sectional SEM images showed distinct phases of the Mg layer on top of the Zn layer. The elemental mapping results further verified the deposition of Zn and Mg layers. The thickness of each metallic layer was intended to be 3 μm, and the line profiles across the metallic film interface acquired by confocal laser scanning microscopy showed that the thicknesses of the Mg, Zn, and Mg/Zn films were close to 3 μm: 2.578 ± 0.386 μm, 2.829 ± 0.101 μm, and 5.370 ± 0.742 μm, respectively (**Figure 4**).

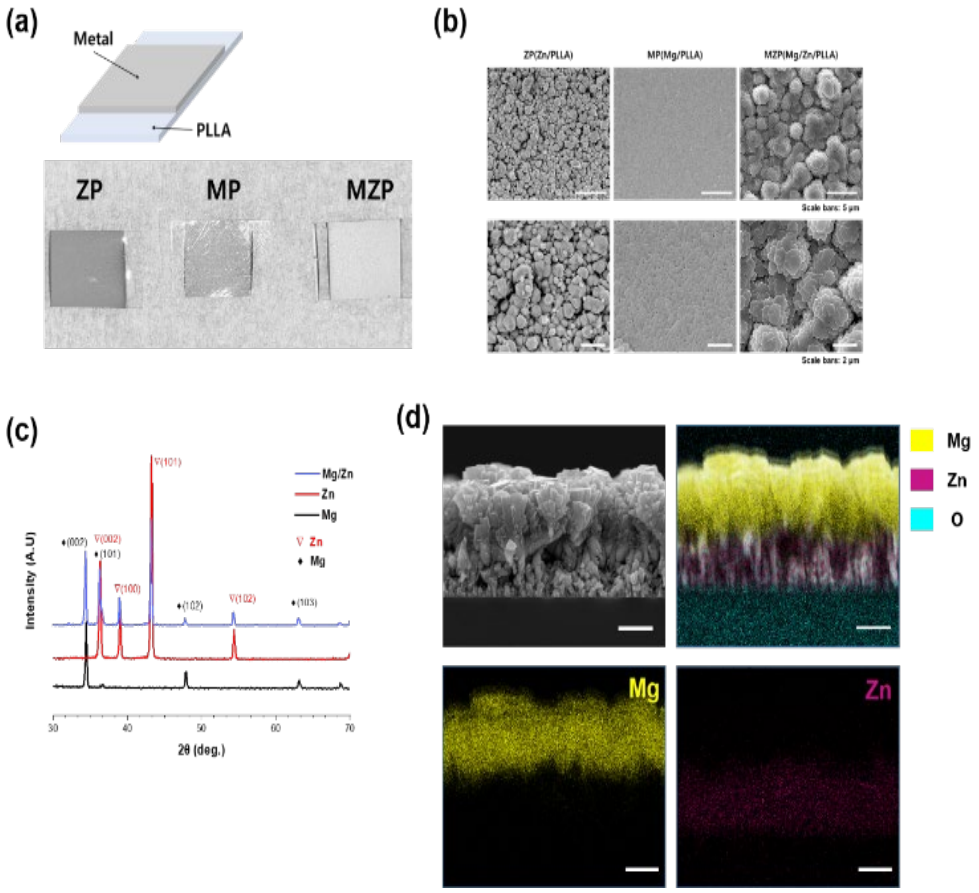

Figure 3. a) Metallic films sputtered on PLLA films, b) SEM images of metal/PLLA hybrid materials, c) XRD spectra of metal on the glass substrate, d) cross-sectional SEM and EDX mapping images of Mg and Zn layer sputtered on the glass substrate (scale bar 2μm).

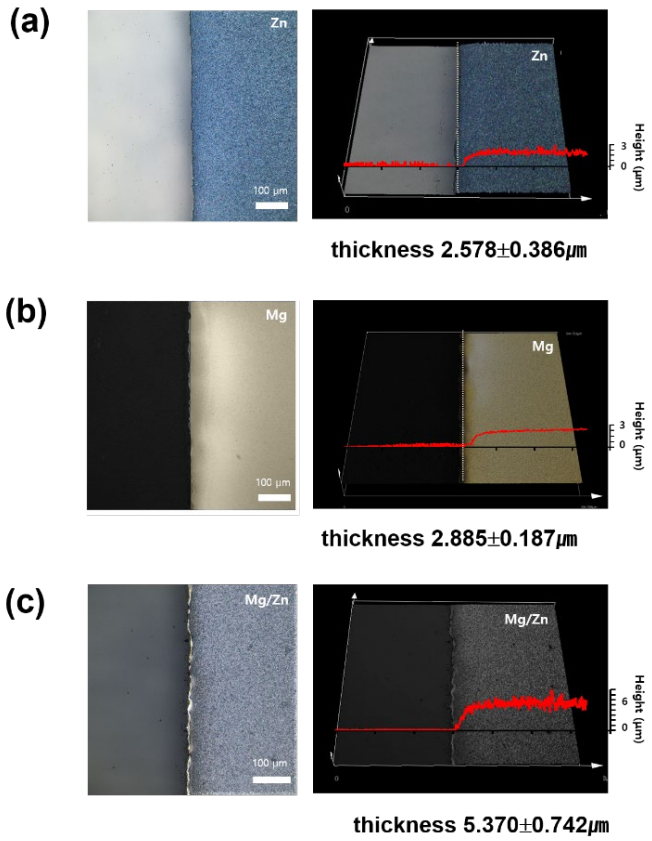

Figure 4. Line profiles of height, thickness values, and 3D images of a) Zn, b) Mg, and c) Mg/Zn films on the glass substrates analyzed by a confocal laser scanning microscope (LSM; LEXT OLS4100, Olympus, Japan) (Mean ± SD n = 3).

2.3.2 Long term immersion test

To evaluate the long-term ROS generation behavior of the hybrid materials, immersion tests were performed for 2 weeks. Long-term immersion tests are frequently used to assess the long-term corrosion behavior of biodegradable metals with the cumulative volume of H_2 as an indication of the change in corrosion behavior [11, 69-70]. However, unlike H_2, ROS are thermodynamically unstable and easily converted to various types of less reactive forms [25]; hence, the cumulative quantity of ROS cannot be an appropriate factor for the calculation of the daily ROS generation rate change during the long-term immersion of biodegradable hybrid materials. Therefore, instead of measuring the ROS concentration of the solution in which hybrid materials had been continuously immersed, we monitored the amount of ROS formed for an hour in fresh PBS using the samples taken out of the immersion solution at a fixed time every day, as described in **Figure 5a**. The variation in the ROS generation capacity for an hour is shown in **Figure 5b** and **5c**. Both MP and MZP samples showed maximum rates of $\cdot O_2^-$ generation on "day 0", the first immersion in PBS for an hour, whereas after 23 h, the ability to generate $\cdot O_2^-$ fell abruptly on "day 1." MP samples generated approximately 15 nmol/cm^2·h of $\cdot O_2^-$ on day 0, and the generation rate decreased to 3.26 nmol/cm^2·h on day 1. A significant amount of $\cdot O_2^-$ was not detected on day 2 because of the complete consumption of Mg between days 1 and 2, resulting in no electron production for the ORR. Our previous studies dealt with artificial galvanic corrosion couples between biometals for ROS generation [23, 60, 71]; however, this study confirmed that the corrosion of a single biodegradable metal can also generate ROS. For MZP samples, the $\cdot O_2^-$ generation rate was 39.9 nmol/cm^2·h on day 0, and this fell to 23.5 nmol/cm^2·h on day 1. However, unlike the MP hybrid materials, because the MZP hybrid materials still had a metallic Zn layer after the Mg film was exhausted, they maintained their $\cdot O_2^-$ generation ability until day 8, as shown in **Figure 5b**. Notably, $\cdot O_2^-$ generation by the MZP hybrid materials on both days 0 and 1 was greater than that of the MP hybrid materials. The galvanic corrosion is generally faster than the corrosion of a single metallic entity [72-73]. As shown in **Figure 6**, the H_2 was generated about 14.34 times more in MZP hybrid materials (0.204 ml/cm^2) than in MP hybrid materials (0.014 ml/cm^2) for 1 h on

day 0. Moreover, the results of ICP-OES denoted how much Mg and Zn were oxidized and released into the solution in which the samples were immersed for 1 h (**Table 1**). When the amount of Mg ions in the solutions of MZP and MP hybrid materials was compared, about 4 times more Mg ions were measured in the solution of MZP where galvanic corrosion occurred. The results of H_2 generation and ICP-OES experimentally revealed that the galvanic corrosion accelerated the corrosion of the Mg layer and the corrosion proceeded more. Therefore, the production amount of electrons available for ORR would be greater with the MZPs. In addition, the corrosion process generating electrons and H_2 evolution and ORR consuming those electrons occurred on the Mg film surface in the MP, whereas electrons were consumed on both the Mg film and the cathodic Zn surface in the MZP. Moreover, as the electrochemical potential gap between pure Zn and the $\cdot O_2^-$ is much smaller than that between pure Mg and the $\cdot O_2^-$, as shown in **Figure 7** [25, 74], it is expected that more $\cdot O_2^-$ molecules are generated on the Zn surface. Regarding the H_2O_2 generation behavior shown in **Figure 5c**, the MP hybrid materials exhibited the same pattern as the $\cdot O_2^-$ generation behavior. However, the H_2O_2 generation rate change from the MZP hybrid materials was very different from that of the $\cdot O_2^-$ for the first two measurements: on day 0, when the $\cdot O_2^-$ generation rate was the highest, the H_2O_2 generation rate was the lowest, (9.5 nmol/cm^2·h) among the values greater than the significant detection range, but increased to 59 nmol/cm^2· h on day 1, and then decreased again to approximately 40 nmol/cm^2· h on day 2 and maintained that level till day 6. Even if this is applied to *in vivo* cases, when the structure of the stents is inserted into the blood vessels, the soft tissue of the vessel wall would tightly surround the stent surface (**Figure 8**). That condition makes the stent strut locally in the closed system, $\cdot O_2^-$ do not turn into H_2O_2 molecules due to a lack of protons. Also, pH change would be insignificant in the system, so the same conditions in **Figure 5c** also happens to *in vivo* environment.

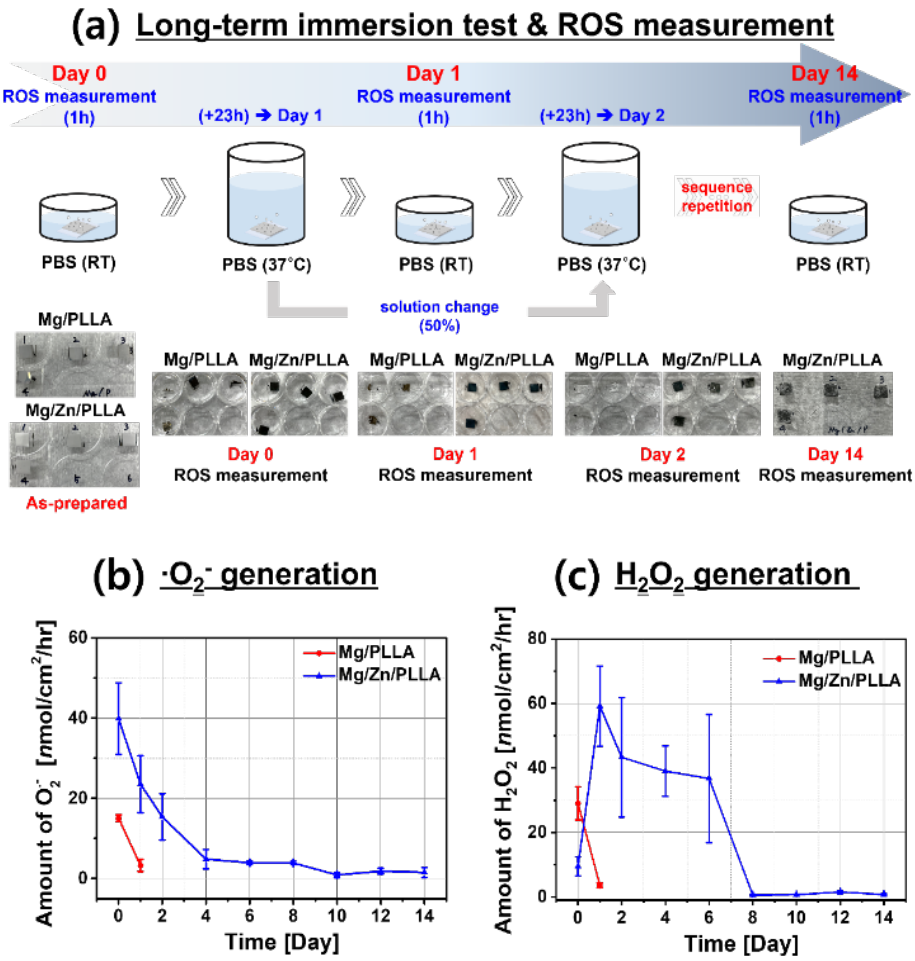

Figure 5. a) Schematic of experimental protocols for long-term immersion test and ROS measurement, b) superoxide anion generation behavior of Mg/PLLA and Mg/Zn/PLLA hybrid materials for 14 days, c) hydrogen peroxide generation behavior of Mg/PLLA and Mg/Zn/PLLA hybrid materials for 14 days. (Mean ± SD n = 4)

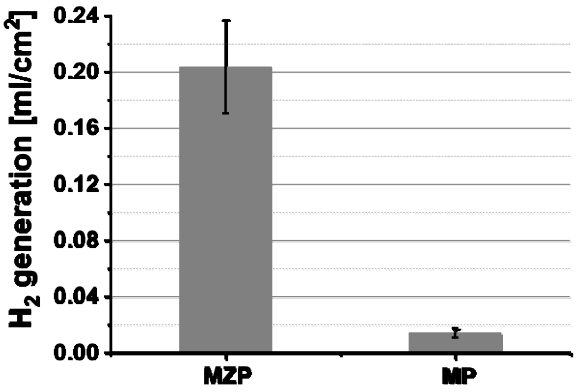

Figure 6. The measurement of hydrogen gas generation amount on the MP and MZP hybrid materials for 1 h on day 0.

Table 1. Analysis of the Mg and Zn ion releasing amount in the PBS solution during immersion testing for 1 h on day 0 by ICP-OES.

Sample	Unit	Mg	Zn
MP	mg/L	3.39	< 0.1
MZP		13.0	< 0.1

* The mark (<) below indicates that the detection limit is not detected by this test method.

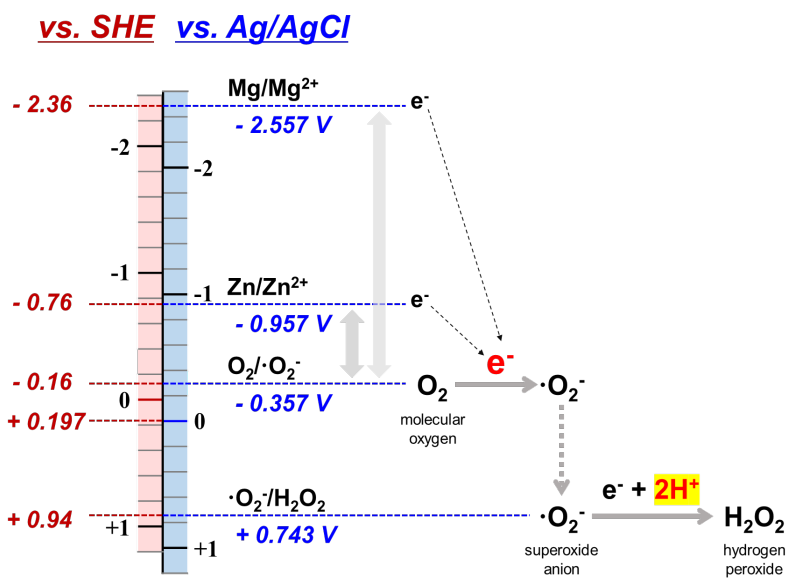

Figure 7. Schematic illustration of ROS generation/conversion reactions and their potential levels together with oxidation of Mg and Zn. (ROS generation and conversion reactions and their potential values)

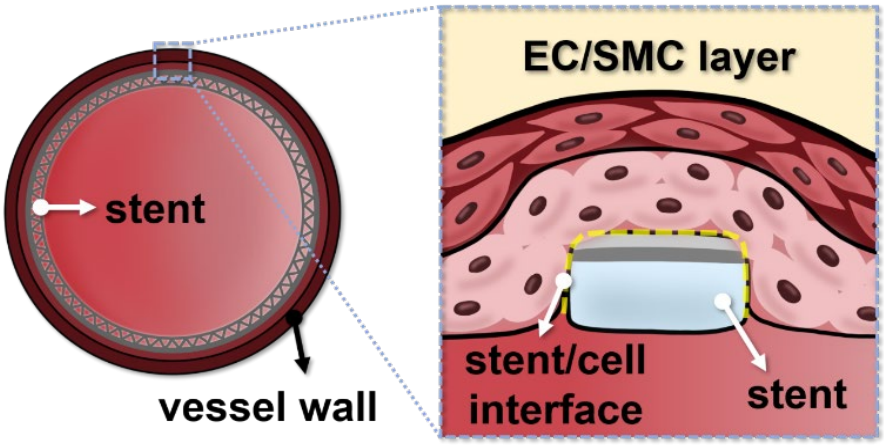

Figure 8. Schematic image of stent inserted blood vessel. After the stent was inserted, because the cell layers are soft enough, the stent tightly fits into the inner vessel wall, then the layers of endothelial cells and smooth muscle cells surround the stent.

This discrepancy can be explained by the stepwise ORR processes. $\cdot O_2^-$ can be produced by the simple addition of one electron to a dissolved oxygen molecule, as shown in **Figure 7**. The addition of another electron, together with two protons (H^+), to $\cdot O_2^-$ can produce a H_2O_2 molecule. On day 0, vigorous corrosion of Mg produced a large number of electrons, which were primarily used to produce H_2 bubbles and partially used to form ROS by ORR. The massive corrosion of Mg and generation of H_2 bubbles resulted in an alkaline environment near the Mg surface [75-76]. **Figure 9a** shows the results of pH variation depending on the system size during the immersion test of MZP hybrid materials for 1 h on day 0. When the MZP sample was immersed in 6 ml of PBS, the pH increased by about 0.66, showing that the surrounding environment was alkalized. On the other hand, the pH values increased only 0.02 in the 100 ml system and the difference elucidated that the pH change occurred very locally. When the pH change around MP and MZP hybrid materials was measured (**Figure 9b**), the pH increased more around MZP where galvanic corrosion occurred than around MP. Then, the number of protons was reduced by about 80% and about 20% around MZP and MP, respectively, during the immersion test for 1h. Therefore, the result would be salient causative that the already formed $\cdot O_2^-$ were difficult to combine with protons and form H_2O_2 due to a lack of protons around MZP. Thus, the generation rate of $\cdot O_2^-$ was at its maximum on day 0, while H_2O_2 generation was inhibited by the shortage of available protons.

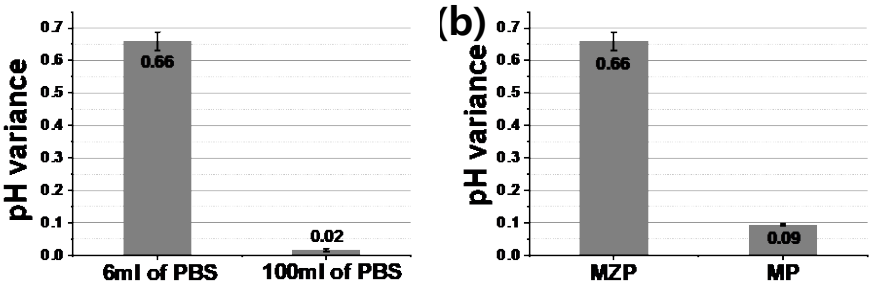

Figure 9. Measurement of the pH variance a) around MZP hybrid materials depending on the system size, and b) around MP and MZP hybrid materials during the immersion test for 1 h on day 0.

On day 1, the Mg films were almost completely consumed, but some island-like regions remained and the corrosion of both these island-like Mg films and the fresh Zn films contributed to the electron supply to the ORR. As the ROS generation ability measurement was performed in fresh PBS, the pH near the metallic film surface did not deviate significantly from 7.4, implying a sufficient number of protons available to convert $\cdot O_2^-$ to H_2O_2 molecules. Therefore, the H_2O_2 generation rate rose to its maximum on day 1 but dropped on day 2 due to the exhaustion of Mg. As the H_2O_2 generation ability in **Figure 5c** from day 2 to day 6 did not show notable fluctuations, it can be inferred that these values are the intrinsic H_2O_2 generation levels of the Zn layer. However, it should be noted that this hypothesis only explains the trend of $\cdot O_2^-$ and H_2O_2 generation rate changes on days 0 and 1 in the finite volume of PBS in vitro. It could not provide quantitative information on conservative molecular tracking, that is, what portion of the $\cdot O_2^-$ had been converted to H_2O_2, water molecules, or other compounds, as $\cdot O_2^-$ generation and H_2O_2 formation were measured independently in different PBS with different individual samples, using different sampling methods and molecular probes. Nevertheless, as stated above, the Zn film alone could generate ROS, similar to the Mg film in the MP samples. Therefore, it can be concluded that galvanic coupling of the metallic bilayer is not indispensable for the artificial ROS generation design. It can be inferred from the generation rate values of $\cdot O_2^-$ after day 8 and those of H_2O_2 after day 6 that Zn films were exhausted after 6 to 8 days of immersion in PBS. Examining the long-term ROS generation behavior and sample images comprehensively, 3-μm thick Mg films were completely corroded within two days, whereas Zn films of the same thickness were exhausted after approximately 5 – 7 days. The ROS generation rate change and total ROS generation time can be determined by the thicknesses of the Mg and Zn films.

2.4 Conclusion

Biodegradable hybrid materials consisting of biodegradable metallic films and PLLA substrates were prepared, and their long-term ROS generation behavior in PBS was monitored for two weeks. Both $\cdot O_2^-$ and H_2O_2 were generated seamlessly even after the complete consumption of the anodic Mg layer in the MZP hybrid materials. $\cdot O_2^-$ and H_2O_2 were formed by the corrosion of a single Mg or Zn layer, meaning that metallic bilayers constituting galvanic corrosion couples are effective but not indispensable for artificial ROS generation design. Therefore, Mg/Zn/PLLA hybrid materials are good candidates for biodegradable hybrid stent materials with ROS functionalization to suppress the risk of in-stent restenosis.

Chapter 3. ROS generation behavior by carious Mg-based alloys

3.1 Introduction

The microstructure, surface morphology, and composition of the Mg surface have a great influence on their corrosion behavior when inserted into the human body [27]. In particular, Mg corrosion is most active in the initial stage, and the initial surface states would be a critical role in the establishment of stable cell-surface bonding [26-28]. The immersion test is the simplest of the in vitro methods for investigating the degradation performance of Mg. Mg generates electrons as it corrodes, and these electrons decompose water to generate H_2 [42, 77]. The corrosion rate of the Mg can be calculated by immersing it in a solution and collecting the H_2 generated by the corrosion reaction [27-28]. In most studies dealing with the corrosion rate of the Mg, only this amount of H_2 generated is explained and analyzed. However, electrons generated as the Mg corrodes can also react with dissolved oxygen in the solution to generate ROS. ROS are actively studied in the field of medical engineering by treating cancer and killing harmful bacteria with their excellent antibacterial activity [42-44]. In addition, they are recently in the spotlight in the fields of catalyst and environment as well [45-46]. For this reason, it has become important to understand the tendency of ROS generation due to Mg corrosion.

In terms of the histology of metals, multi-phase alloys inevitably produce a cathode area and an anode area [78]. Due to the potential difference of each phase, micro galvanic corrosion is generated between phases [79]. Then. electrons move from the anode region (low potential) to the cathode region (high potential), and the aforementioned two reactions mainly occur on the cathode surface (**Figure 10**) [80]. Galvanic corrosion has been studied to generate more electrons as the corrosion rate is accelerated than that of single-phase metal corrosion, and as a result, it induces more generation of ROS [23, 81] as well as H_2 [82-83]. Even, the thick oxide layer produced by the active corrosion reaction on the corroded surface has been considered to prevent dissolved oxygen from accessing the surface, creating an environment in which it is difficult to react with electrons [84-87]. However, in our previous paper, the amount of $\cdot O_2^-$

generated on the first day of the Mg single-thin film was sufficiently large to that of the MZP sample made by the artificial galvanic system [24]. In addition, even when only the Zn thin film remained after Mg was completely melted, ROS was actively generated. In other words, it suggested that ROS could occur a lot even in an environment where a little electron is supplied. Through this, it was hypothesized that the generation of ROS would be an important factor in the intrinsic properties of metals, as well as the supply of electrons.

Herein, we tried to investigate how large the amount of the electron supply, which is represented by the corrosion rate, is a factor in the generation of ROS in the initial corrosion stage of Mg-based alloys. In addition, based on the metallographic histology, the influence of the microstructure and surface composition of the Mg-based alloys on ROS generation was also studied. The corrosion tendency and ROS generation quantity of Mg-based alloys with different corrosion rates were measured for 1h. In addition, by supplying a certain number of electrons to minimize the influence of the natural corrosion rate that cannot be overcome, the change in the amount of ROS generated when the electron supply rate is increased was measured. Based on the results, the causes involved in ROS generation during immersion were thoroughly analyzed based on metallographic factors.

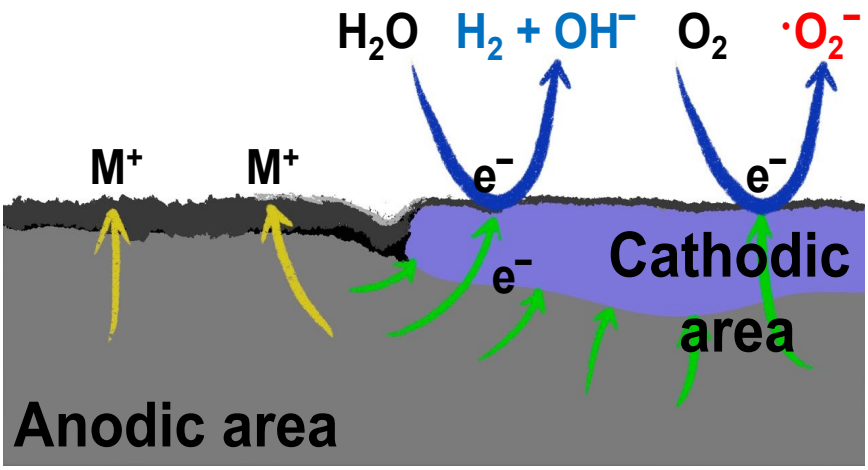

Figure 10. Schematic illustration of micro galvanic corrosion mechanism on the surface of the Mg-based alloy.

3.2 Experimental procedures

3.2.1 Specimen preparation

Mg - 5wt% Ca, Mg - 5wt% Ca - 1wt% Zn and Mg - 3wt% Zn alloys were prepared by melting high-purity Mg (99.99%, provided by U&i Corp.), Ca (99.5%, procured from RND Korea Corp.), and Zn (99.5%, procured from RND Korea Corp.) in a steel crucible (STS430) at 750 °C under argon (99.999%) atmosphere as a protective gas. The molten Mg, Ca and Zn were stirred for 15 min, followed by 1 min of stabilization. The molten mixture was then poured into a room temperature (RT) mold (STS430 steel). Two different ways of the Mg - 3wt% Zn alloy billets were prepared; one was cast as a second phase precipitated as a multi-phase alloy, and the other was homogenized at 400 °C for 24 h following ice water quenching as a single-phase alloy. The Mg alloy billets were machined to have dimensions of Φ 50 mm × 50 mm for hot extrusion. The extrusion temperatures of Mg-Ca alloys, Mg -3wt% Zn alloys and pure Mg were 400 °C, 350 °C and 200 °C, respectively. A curved die was employed with an extrusion ratio of 39:1, and the extrusion ram speed was 0.1 mm/s. Crucially, each billet was heated to the desired extrusion temperature before extrusion. Then, every alloy was obtained as coin specimens with dimensions of Φ 8mm × 0.8mm.

3.2.2 ROS measurement

The dye products were used as the indicator of ROS generation. $\cdot O_2^-$ were detected by measuring the absorbance of the XTT formazan dye at a GloMax® Discover Microplate Reader (Promega, USA). After immersion of the coin samples in the XTT solution, which was the mixture of the XTT sodium salt (2,3-bis-(2-methoxy-4-nitro-5-sulfophenyl)-2H-tetrazolium-5-carboxanilide inner salt, Sigma, USA) in PBS (pH 7.4, Welgene Inc.) solution and PMS (N-methyl dibenzopyrazine methyl sulfate, XTT cell proliferation kit, abcam, UK) for 1 h, a sampling solution was taken in the 96 microplate, and the absorbance of each sample was measured at the 450 nm of wavelength. Then, the quantitative concentration of $\cdot O_2^-$ was calculated by converting qualitative absorbance values with the Beer-Lambert law.[24]

A fluorometric H_2O_2 assay kit (Sigma, USA) was used to measure the H_2O_2 generation.

After immersing the samples in PBS solution, the solution was collected at 1 h and mixed with the H_2O_2 assay reagent. The mixtures were measured the intensity of the fluorescence product (resofurin) at λ_{ex} = 540 nm and λ_{em} = 590 nm at a microplate reader. The fluorescence intensity was calculated from a standard curve of the known concentration of H_2O_2.

3.2.3 H_2 measurement

H_2 measurements were conducted in a 1 x PBS solution in a water bath set to 37 ± 5 °C. The coin specimens were drilled as a Φ1 mm hole in the center to hang them inside of cylindrical holder. The surfaces of the specimens were ground with SiC sandpaper up to 2000-grit and cleaned with alcohol for 3 min in a sonic bath followed by air gun drying. The ratio of the total surface area of the samples to the volume of the solution was set to approximately 1.70 mm^2/ml. The H_2 evolution volume rates as functions of time were measured and calculated by monitoring the height of the solution in the funnel system for 1h.

3.2.4 Electrochemical test

Five kinds of coin specimens were attached with electrical lines, and the attaching part was thoroughly enveloped by epoxy resin. A potentiostat (VersaSTAT 3, AMETEK, USA) was used for the measurements and contribution of electrochemical properties of each coin specimen electrode such as the open circuit potential (OCP), the potential level measurement, and the amount of the ROS generation during the application of the cathodic current in PBS solution for 1 h. The coin specimen electrodes, Ag/AgCl, and Pt plate were the working electrode, the reference electrode, and the counter electrode, respectively.

3.2.5 Characterization

The microstructures and surface characteristics of both bare and corroded specimens were observed by field-emission scanning electron microscopy (FE-SEM; Inspect F50, FEI). The corroded specimens by immersion were coated with a thin layer of platinum before observation. The energy dispersive X-ray spectroscopy (EDX; Inspect F50, FEI) was used for elemental analysis. Phase analysis of bare and corroded Z3M samples were performed using X-ray

diffraction (XRD; D8 Advance, Bruker) with Cu Kα radiation (λ = 1.5406 Å) operated at 40 kV and 40 mA. The surface chemical compositions of Z3M after the immersion were investigated using X-ray photoelectron spectroscopy (XPS: NEXSA, Thermo Fisher Scientific) with a monochromic Al Kα source at 1486.6 eV. The cross-section structures of oxide layer on the specimens were observed by the transmission electron microscopy (TEM; Tecnai, FEI, USA). The TEM samples were prepared using a dual-beam focused ion beam (FIB; Helios G4 HX, FEI, USA).

3.2.6 Oxide layer and ZnO model test

The RF magnetron sputter (Korea VAC-TEC Co. Ltd., Republic of Korea) equipped with ZnO (4N, VTM Co, Republic of Korea) and MgO (4N, VTM Co, Republic of Korea) sputter targets was used for the deposition of each metal oxide layer on the masked pure Mg specimens. Two types of samples with different thicknesses of ZnO layers were prepared by varying the deposition time. Targets were sputtered under the base pressure of 1.7×10^{-6} mTorr and process pressure of 3 mTorr. The Ar flow rate was 10 standard cubic centimeters per minute. The deposition rate of ZnO was approximately 3.17 nm/min, with a sputtering power of 60 W. The amount of ROS generation of the samples was measured under the cathodic current in PBS solution for 1 h.

3.3 Results and Discussion

3.3.1 Mg-based alloys

Based on the corrosion rate of the pure Mg, two types of multi-phase alloys (Mg - 5wt% Ca and Mg - 5wt% Ca - 1wt% Zn) with a faster corrosion rate, and single and multi-phase alloys of the Mg - 3wt% Zn with a slower corrosion rate were prepared [10, 19, 88-89]. The Mg alloys are denoted as pM, CZ50, CZ51, Z3S, and Z3 M, corresponding to pure Mg, Mg - 5wt% Ca, Mg - 5wt% Ca - 1wt% Zn, Mg - 3wt% Zn alloy with single-phase and multi-phase, respectively. The surfaces of five coin specimens were observed in the backscattered electrons (BSE) mode of the SEM, and each phase was defined through the EDS (**Table 2**). In the case of the CZ50 sample, a bright Mg_2Ca phase was present as a wave pattern in the dark Mg matrix (**Figure 11a i**) [88-90]. The CZ51 specimen, which additionally contains 1 wt% Zn, had a brighter island region ($Mg_6Ca_2Zn_3$ phase) in a pattern similar to that of the CZ50 (**Figure 11a ii**) [10, 16]. **Figure 11a iii** is an SEM image of the pM, which demonstrates that it is a single phase. In the case of the Mg-Zn alloys, it was confirmed that the Z3M specimen showed a rippling pattern of the MgZn phase and was multi-phase, whereas the Z3S specimen was single-phase (**Figure 11a iv** and **11v**) [19, 91]. The XRD patterns of the five bare specimens in **Figure 11b** showed distinct Mg peaks from all five samples and Mg_2Ca peaks from CZ50 and CZ51. It is estimated that the Zn content of 3wt% is too low to represent the peaks of the MgZn phase [19, 92].

Table 2. The EDS atomic percentage of each phase on the bare specimens.

Specimen	Phase	Mg	Ca	Zn	O
CZ50	α-Mg	100			
	Mg_2Ca	79.4	16.2		4.3
CZ51	α-Mg	100			
	Mg_2Ca	66.2	26.8	0.8	6.2
	Mg_6Ca_2Zn3	78.6	8.7	8.9	3.7
pM	α-Mg	100			
Z3M	α-Mg	100			
	MgZn	98.4		1.6	
Z3S	MgZn	98.8		1.2	

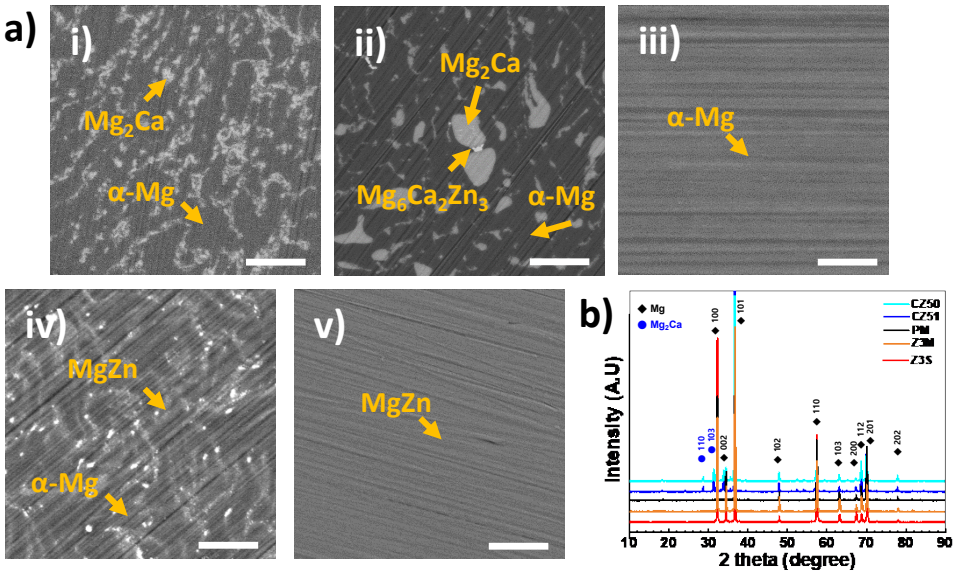

Figure 11. (a) SEM images of i) CZ50, ii) CZ51, iii) pM, iv) Z3M, and v) Z3S, (b) XRD spectra of bare specimens. (scale bar: 20μm)

3.3.2 Immersion test

The Mg-based alloys corrode and generate electrons, and the amount of H_2 generated could be an indicator of the degree of corrosion. **Figure 12a** shows the corrosion results of five specimens by collecting H_2 generated in PBS solution for 1 h. The corrosion rate is decreases in the order of CZ50 > CZ51 > PM > Z3M > Z3S as expected. Galvanic corrosion is the main corrosion mechanism of CZ50, CZ51, and Z3M due to their 2nd phase, such as Mg_2Ca for CZ50 and CZ51 alloys, and MgZn phase for Z3M alloy. Especially, in the case of the CZ51, the potential difference between the Mg_2Ca phase and α-Mg phase was decreased by adding Zn [11]. It was indicated that the proper addition of Zn could minimize the galvanic corrosion by controlling the potential of galvanic cell [11, 93-94]. The addition of a small amount of Zn to Mg matrix increases the corrosion resistance [19, 95]. The H_2 generation amount of Mg-Zn alloys is generally less than that of Mg-Ca alloys. In the case of the Z3S, the complete dissolution of Zn in α-Mg phase especially led to the removal of galvanic cells and restrained the micro galvanic corrosion. Then, the corrosion rate of the Z3S shows the highest corrosion resistance.

The amount of ROS generation of the five specimens was measured during immersion in PBS solution for 1 h **(Figure 12b)**. The amount of $\cdot O_2^-$ interestingly was inversely proportional to the amount of H_2 generated, which was a corrosion tendency. In other words, CZ50, which had the fastest corrosion, produced the lowest amount of $\cdot O_2^-$, and Z3S, which had the slowest corrosion, generated the most $\cdot O_2^-$. On the other hand, since the amount of the H_2O_2 generation did not show a clear trend, the measurement of $\cdot O_2^-$ would be considered a better index in judging the ORR possibility of the specimens. The amount of H_2 and ROS generated demonstrated no relationship between the number of electrons supplied by corrosion and the amount of ROS generation.

The different tendencies of H_2 and ROS generated by corrosion of the specimens could be explained in the competition of surface reactions between water decomposition and oxygen reduction. The CZ50 responsively and vigorously produced the H_2 as soon as immersed in PBS solution. Its excessive corrosion depleted the chance for dissolved oxygen to react with electrons on the surface (**Figure 12c**). On the other hand, Mg-Zn alloys, which have high

corrosion resistance and less active water decomposition reaction, could generate a lot of ROS, the result of the ORR, because there was sufficient space for dissolved oxygen molecules to react with electrons on the surface (**Figure 12d**). These results indicated that water decomposition prevailed over ORR in surface competition.

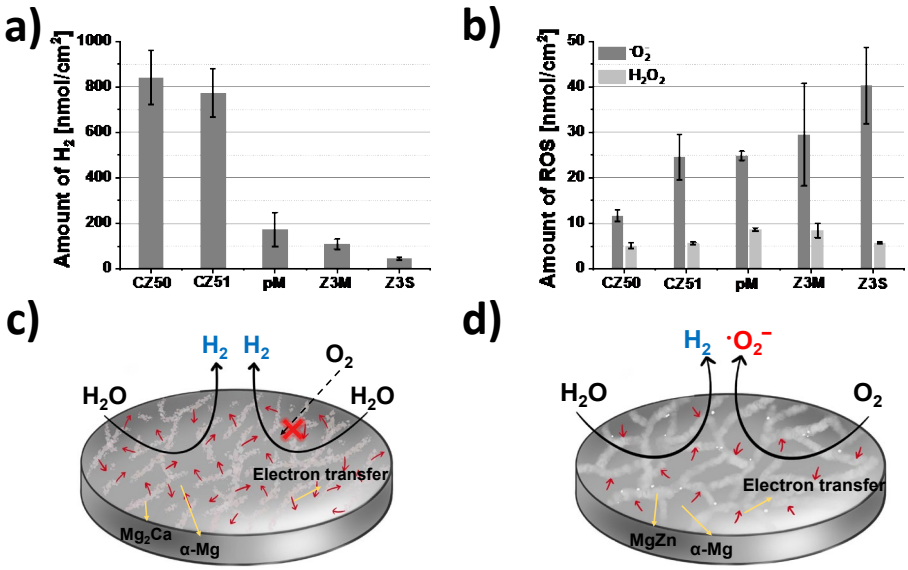

Figure 12. The amount of a) H_2 generated and b) ROS generation of the five specimens in PBS solution for 1 h. Schematic illustration of the cathodic reaction on the c) CZ50 and d) Z3M surface during the immersion test.

3.3.3 Cathodic current test

When a cathodic current is applied, the alloys can participate in surface reactions with more electrons than in natural corrosion. As shown in **Figure 13a**, when electrons were artificially supplied to the alloy specimens, the amount of ROS generation was measured and the movement of electrons was analyzed. The amount of H_2 generated from the natural corrosion of pure Mg in PBS solution for 1 h was about 3.45 μl/cm^2. At this time, the number of electrons participating in H_2 generation was converted into - 0.01 mA of the current. When the current was applied to five specimens in PBS solution for 1 h, each potential descended in the cathodic direction, indicating that the electrons flowed from the potentiostat to the specimen as the cathodic current (**Figure 13b**). The artificial supply of the electrons to five alloy specimens shows interesting results for ROS generation. In the case of $\cdot O_2^-$, the generation amount of Mg-Ca alloys and pure Mg was decreased compared to those of general immersion, whereas the amount of Mg-Zn alloys increased, as shown in **Figure 13c**.

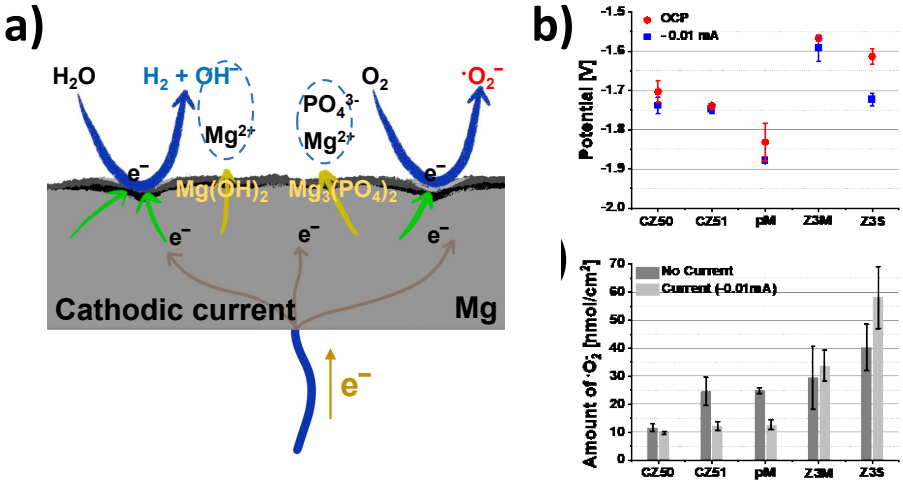

Figure 13. a) Schematic illustration of the corrosion of the pure Mg under a cathodic current, b) the potential difference under a cathodic current of the five specimens in PBS solution for 1 h, c) the amount of ROS generation of the five specimens under a cathodic current in PBS solution for 1 h.

The cathodic protection would be the causative factor in the diminution of the amount of $\cdot O_2^-$ when the cathodic current was applied to Mg-Ca alloys and pure Mg which were actively corroded in the immersion test. Electrons supplied from the potentiostat are consumed to prevent the ionization of the anodic area on the specimens [96]. Therefore, the absolute number of electrons participating in the surface reaction in CZ50 was descended compared to the immersion test (**Figure 14a**). The amount of the magnesium ions dissolved in the PBS solution was significantly reduced when the cathodic current was applied compared to the immersion test in the inductively coupled plasma (ICP) measurement (**Figure 14b**). Additionally, the O/Mg atomic ratio could be indirectly deduced as an indicator of the oxide layer on the specimens [85]. Since the thickness of the oxide layer analyzed by the EDS was thinner than that of the immersion test, it was demonstrated that the corrosion of the specimens was protected when electrons were supplied from the potentiostat (**Figure 14c**). Contrary to the results of the above-mentioned oxide layer research [84-87], it was considered that there were other factors besides the corrosion rate of the alloys because the amount of ROS generated was reduced even in the thin oxide layer.

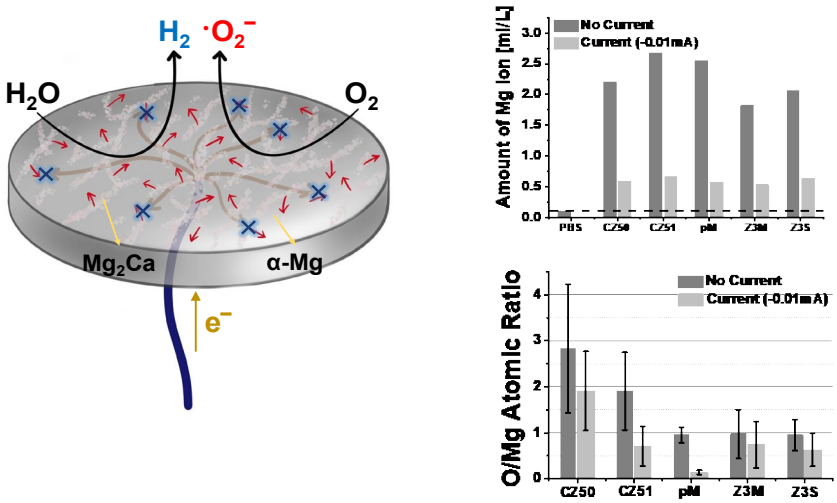

Figure 14. a) Schematic illustration of the surface reaction in CZ50 under a cathodic current, b) the Mg ions releasing amount in PBS solution during immersion test and cathodic current test by ICP-OES, c) the O/Mg atomic ratio after immersion test and cathodic current test by EDS analysis

The increase in ROS generation of Mg-Zn alloys is noteworthy. The value of the cathodic current was calculated on the basis of the natural corrosion of pure Mg in PBS solution for 1 h. Therefore, in the case of Mg-Zn alloys, the electrons were oversupplied compared to the immersion test. The extra electrons participated in the cathodic protection, but they seemed to have more affinity for the oxygen reduction reaction to generate the ROS (**Figure 15a**). The reason that the Mg-Ca alloys and the Mg-Zn alloys showed different ROS generation behavior under the cathodic current applied could be the influence of the exposed surface constituent. The alloys inevitably form an anodic phase and a cathodic phase, and micro galvanic corrosion occurs while electrons are generated in the anodic phase and supplied to the cathodic phase. Specifically, the Mg_2Ca phase including Ca (low reduction potential) becomes the anode, and the α-Mg matrix becomes the cathode in the CZ50 specimen. In the case of CZ51, the α-Mg matrix phase rather than $Mg_6Ca_2Zn_3$ and the Mg_2Ca phase rather than the α-Mg matrix tend to be anodic areas [11, 63, 94]. On the other hand, in the case of Mg3Zn alloys, the α-Mg matrix becomes the anode, and the MgZn phase containing Zn (high reduction potential) becomes the cathode [63]. The division of the cathodic and anodic areas is due to the difference in the potential of each phase in the alloy. As shown in **Figure 15b**, the potential of the Mg_2Ca phase would exist between the OCPs of pure Mg and Ca, and electrons generated in the Mg_2Ca phase and the α-Mg matrix of CZ50 and CZ51 specimens are likely to be supplied to the H_2 generation [11]. Like the corrosion mechanism of pure Mg, the Mg_2Ca phase could participate in the H_2 generation as a local cathode while also serving as an anode under the influence of the negative difference effect (NDE) [63, 97]. On the other hand, Cao et al measured the corrosion potential of Mg-Zn alloys according to the amount of Zn in their study, and the alloys with a large amount of Zn were closer to the potential of pure Zn [98]. Therefore, it was expected that the potential of the MgZn phase in the Z3M and Z3S specimens would be closer to the potential of the pure Zn, and the potential would be preferred to supply electrons to the ROS generation. These denoted that the ROS generation would be more influenced by the potential of the cathodic phase of each specimen than the number of electrons provided by corrosion.

Another difference in surface composition could be made by the oxide layers on the specimens during immersion in PBS solution. Oxide layers on the surface are naturally formed

in the process of metal corrosion. The representative oxide layers of pure Mg and Mg-based alloys are MgO and $Mg(OH)_2$ [76, 99-100]. On the other hand, in the case of Mg-Zn alloys, $Zn(OH)_2$ is formed in the Zn-rich area, followed by the formation of a more stable form of ZnO [101-103]. ROS generation by especially ZnO has been studied in various fields, such as biomaterial, environmental, catalyst, etc [104-106]. Since ZnO has the properties of an n-type semiconductor, if a cathodic current is applied to supply electrons, the electrons would be provided to the conduction band of ZnO [35, 107]. As shown in **Figure 15c**, the conduction band of ZnO is very closely overlapped with the ORR potential for generating $\cdot O_2^-$, so it is advantageous for supplied electrons to generate $\cdot O_2^-$ of ROS [62, 108-110]. On the other hand, the H_2 evolution reaction by water decomposition is more dominant in the potential of the conduction band of $Mg(OH)_2$ [107, 111]. In Mg-Zn alloys, especially in Z3S without galvanic corrosion, more ROS occurred because the oxide layer of ZnO was more even on the surface than that in Z3M. Interestingly, the amount of $\cdot O_2^-$ generated in Mg-Zn alloys was increased under the cathodic current applied in spite of the cathodic protection compared to that of the immersion test, which means that the supply of electrons affects the amount of ROS generation to some extent. However, the cathodic current test result of the Mg-Zn alloys would be good proof that the intrinsic properties of the alloy surface are a more important factor on the ROS generation.

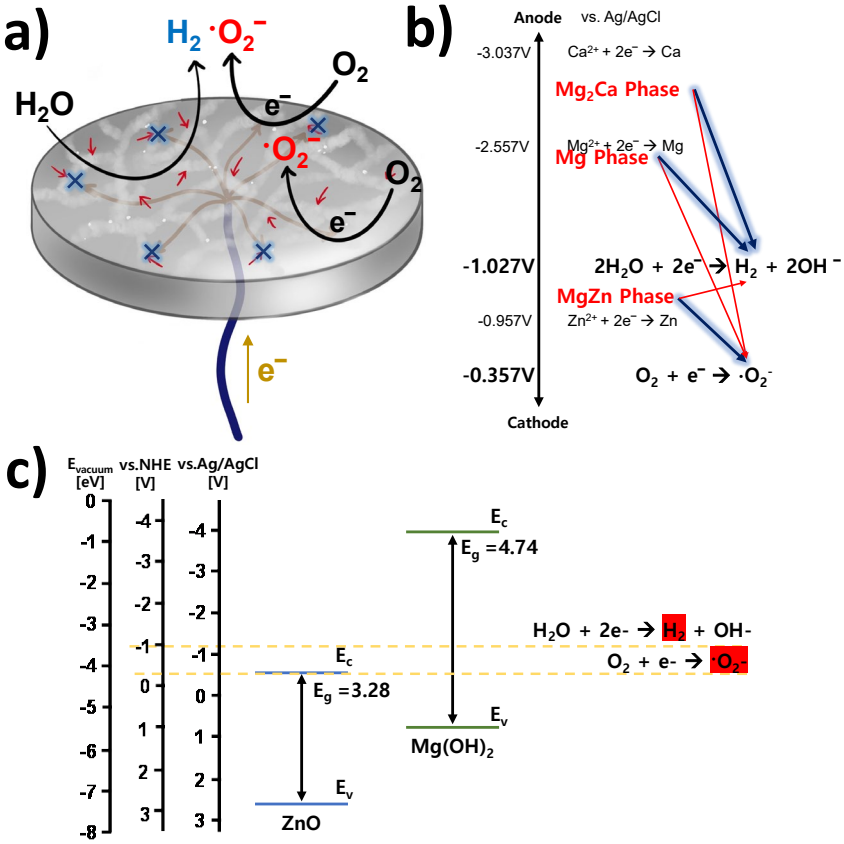

Figure 15. a) Schematic illustration of the surface reaction in Z3M under a cathodic current, b) schematic graph of the potential values of H_2/ROS generation reactions and of each phase in CZ50 and Z3M, c) schematic graph of the band gap of ZnO and $Mg(OH)_2$ as the representative oxide layers.

3.3.4 Surface analysis of corroded Z3M

In order to confirm the presence of ZnO, surface analysis of the oxide layer based on Z3M was performed. Looking at the cross section of the sample, the elements of O and P formed oxide layers where Mg was dissolved (**Figure 16a i** and **16a ii**). The thickness of the oxide layer was about 90 nm, and when a cathodic current was applied, it formed thinner (**Figure 16b ii**) than the immersion test sample (**Figure 16b i**), showing that less corrosion occurred due to cathodic protection.

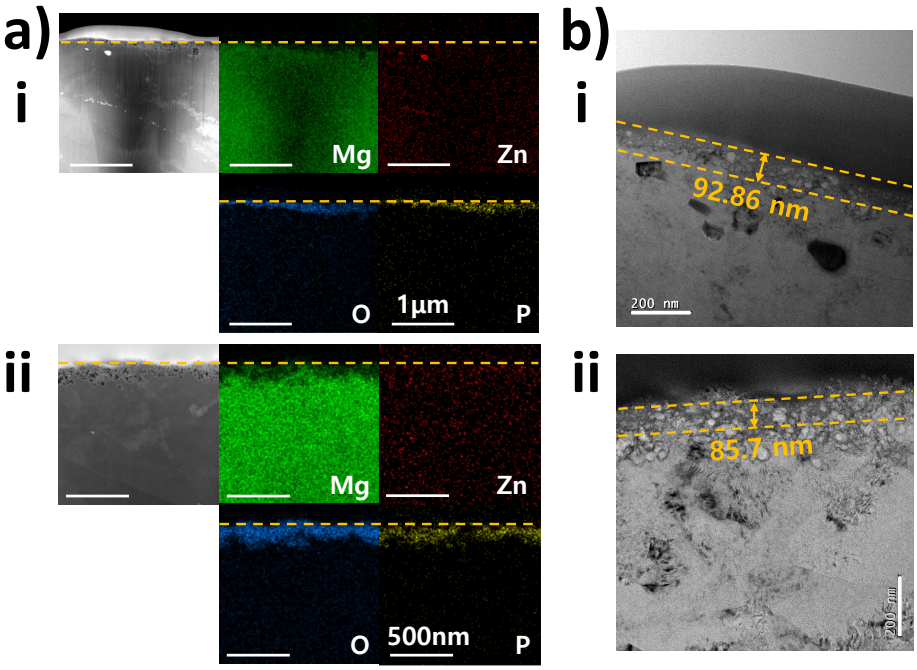

Figure 16. TEM images of a) the cross-section EDS analysis, and b) the thickness of the oxide layer on the corroded Z3M surface in i) immersion test and ii) cathodic current test.

Components on the oxide layer were analyzed by XPS spectrum and XRD patterns. Looking at **Figure 17a**, Zn and O peaks can be seen on the surface. In particular, the presence of Zn 2p, which is a criterion for confirming the existence of ZnO, was confirmed to show the possibility that ZnO exists [112-113]. When a cathodic current was applied compared to the Zn 2p peak in the sample of the immersion test, the Zn 2P peak had more noise and lowered intensity, indicating that the surface was unstable (**Figure 17b i** and **17b ii**).

In the XRD patterns, peaks of various corrosion products such as $Mg(OH)_2$, MgO, $MgCl_2$, and PO_4^- could be seen (**Figure 17c**). Magnesium alloys typically form oxide layers of $Mg(OH)_2$ and MgO. These can be changed to $MgCl_2$ by Cl^- ions in the PBS solution, and the dissolved magnesium ions can form $MgCl_2$ with Cl^- ions directly. Also, cations in PBS and Mg ions dissolved in PBS can combine with phosphate ions and form a phosphate layer. Unlike $Mg(OH)_2$/MgO layers, the phosphate layer is not decomposed by Cl^-, and is easy to crystallize as showing distinct peaks in XRD patterns [26, 28, 114]. In fact, amorphous regions that were not visible on the bare surface were seen in the immersed samples. This result could also be seen in the TEM images, where small lattices were seen between the very amorphous structures (**Figure 17d i** and **17d ii**). In particular, in XRD patterns, peaks showing the presence of ZnO came out at about 34° and 36°, confirming that ZnO exists on the corroded surface of Z3M [115-116].

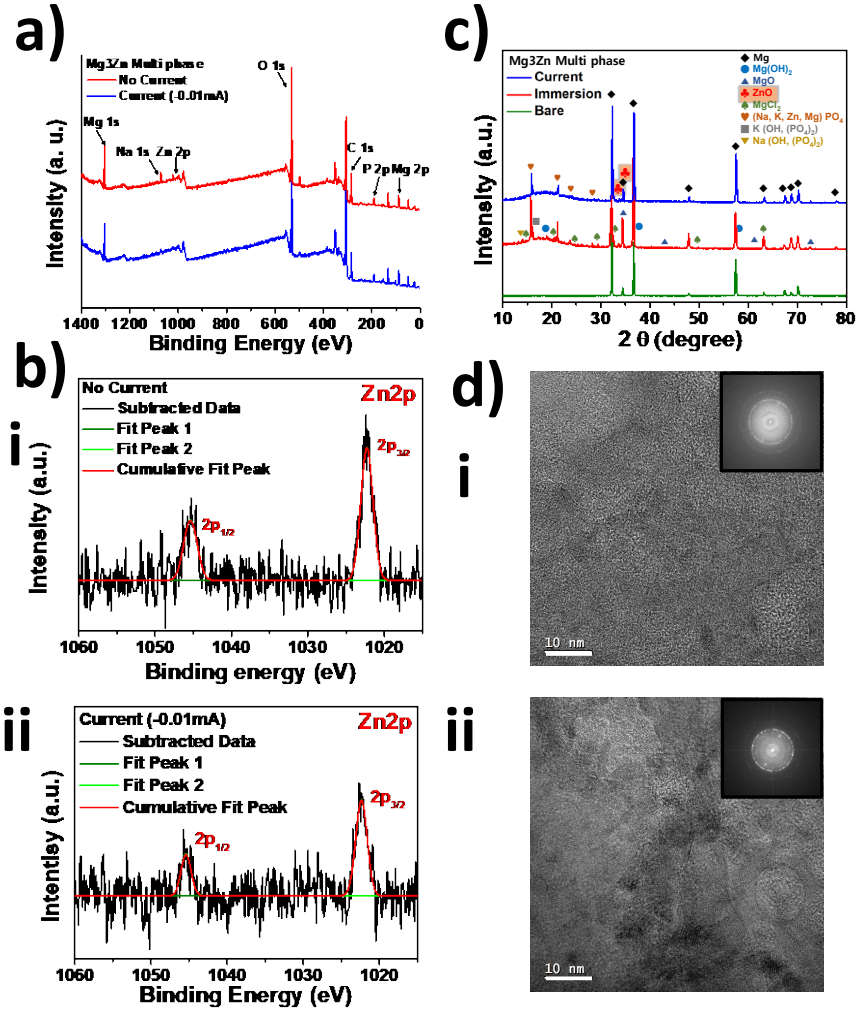

Figure 17. a) XPS survey spectrum of the corroded Z3M surface, b) high-resolution deconvoluted XPS spectra for Zn2P on the corroded Z3M surface in i) immersion test and ii) cathodic current test, c) XRD pattern of the bare and corroded Z3M specimens, d) TEM images and experimental SAEDs collected on the oxide layer of the corroded Z3M in i) immersion test and ii) cathodic current test.

3.3.5 Oxide layer and ZnO model test

Two types of oxide layers were simulated to examine the difference in ROS generation depending on the oxide layers. The thickness of 90 nm ZnO and MgO were separately deposited on pure Mg, and a cathodic current was applied to measure the amount of ROS generated for 1 h. (**Figure 18a**) MgO generated a smaller amount of ROS than pure Mg, but ZnO produced a much higher amount of ROS (**Figure 18b**). Looking at the bandgap of the two metal oxides, unlike the conduction band of ZnO that overlaps with the ROS generation potential, the conduction band of MgO is very high, so the supplied electrons could have participated in other reactions besides ROS [35, 107, 117-119]. Through this experimental result, it was shown that ZnO is more advantageous for ROS generation than other oxides.

Meanwhile, for a more accurate demonstration, Z3M was simulated and ROS generation according to the presence of ZnO was measured. The distribution of the MgZn phase on the Z3M specimen surface was quantified using ImageJ software, and about 30% of the MgZn phase was on the specimen surface. (**Figure 18c**) ZnO was deposited on an area of about 30% on the pure Mg surface using RF magnetron sputtering. When ZnO was deposited on the pure Mg surface for 30 m, the coated area appeared bluish (30% ZnO_30min, **Figure 18e i**). Based on the TEM images, the ZnO coating layer was coated to a thickness of about 90 nm, simulating the oxide layer made by immersion for 1 h. (**Figure 18d**). The sample deposited for 1 m (30% ZnO_1min, **Figure 18f i**) was fabricated to prove the effect on ROS generation when ZnO exists in the form of a cluster rather than a clear layer. Since the ZnO coating layer was very thin, the region could not be clearly identified with the naked eye.

After measuring the amount of ROS generation by supplying a constant cathodic current in PBS solution for 1 h, the pure Mg region was darkened on the surface of the 30% ZnO_30min sample (**Figure 18e ii**). The 30% ZnO_1min sample, in which the ZnO region was not visible, also appeared the ZnO coating layer clearly, showing clearly galvanic corrosion between the pure Mg and the ZnO coating area (**Figure 18f ii**). As a result of measuring the amount of ROS generated, about 5 times more $\cdot O_2^-$ were generated in the 30% ZnO_30min sample with a ZnO layer of 90 nm compared to pure Mg (**Figure 18g**). In addition, even in the 30% ZnO_1min sample in which a precise layer was not formed, the amount of $\cdot O_2^-$ was remarkably increased

just by the presence of ZnO. The ZnO model test showed that ZnO could produce more ROS if it existed on the Mg surface, regardless of whether ZnO existed in the form of a clear layer or cluster.

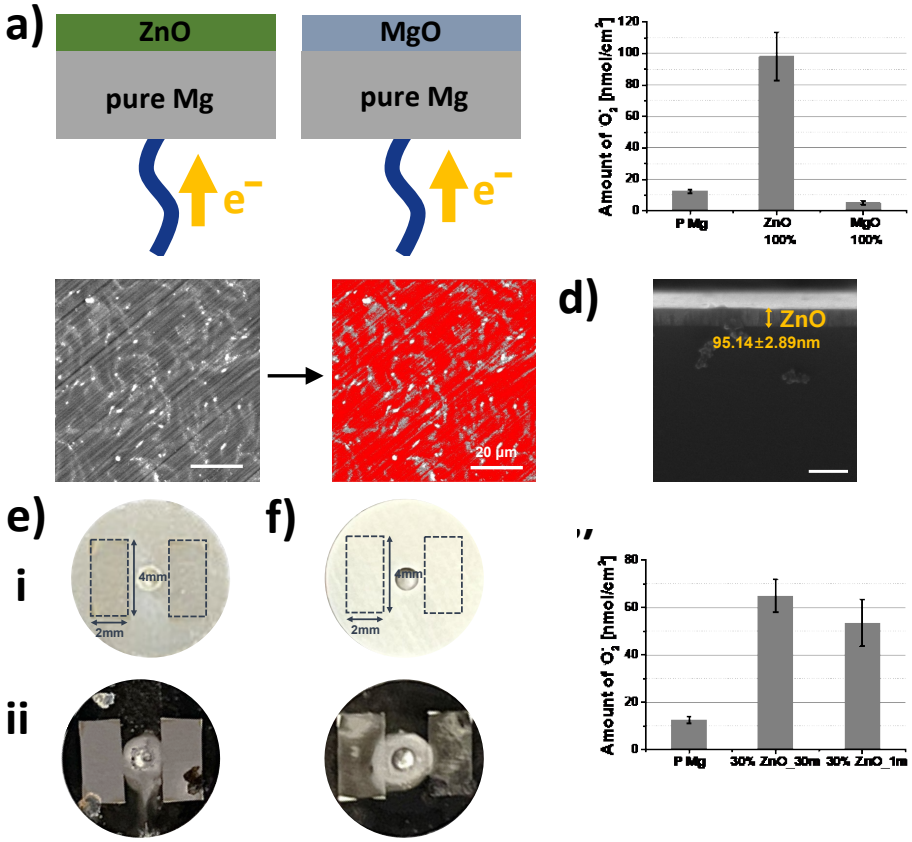

Figure 18. a) Schematic illustration of oxide layer model test, b) the amount of ROS generation in oxide layer model test under a cathodic current in PBS solution for 1 h, c) the process by ImageJ software to measure the area fraction of Zn-rich regions on Z3M specimen, d) the cross-section SEM image of ZnO layer sputtered on pM specimen, sample images of e) 30% ZnO_30min and f) 30% ZnO_1min i) before and ii) after ZnO model test, g) the amount of ROS generation in ZnO model test under a cathodic current in PBS solution for 1 h.

3.4 Conclusion

The number of electrons by corrosion rate has been considered the most important factor in ROS generation. When measuring the actual amount of H_2 generated, the alloys with a fast corrosion rate generated more H_2. However, the amount of ROS generation had no correlation with the corrosion rate. At this time, it was shown that the $\cdot O_2^-$ formed by the reaction of dissolved oxygen with one electron was a better index to explain the ROS generation mechanism than H_2O_2. Although it is difficult to provide a direct rationale for the Mg-Ca alloys that exhibited a fast corrosion rate, it could be inferred that the water decomposition reaction was more dominant in the surface reaction competition. Since the corrosion rate could not be overcome as an intrinsic property of the alloys, the ROS generation behavior was investigated by supplying the same number of electrons. When a cathodic current was supplied based on the number of electrons generated during the natural corrosion of pure Mg in PBS solution for 1 h, the ROS generation of Mg-Ca alloys with fast corrosion decreased, while that of Mg-Zn alloys with slow corrosion increased. This suggests that although the supply of electrons affects ROS generation to some extent in the appropriate range, the more ROS generation in the region where MgZn is the cathode is related to the surface properties. This was confirmed through the oxide layer and the ZnO model tests. As a result, it was proved that the type of cathodic phase and the oxide film formed on the surface, that is, the intrinsic properties of the alloy surface, are the most important factors for ROS generation.

Chapter 4. Biodegradable Mg Electrodes for Iontophoretic Transdermal Drug Delivery

4.1 Introduction

Transdermal drug delivery (TDD) is a painless method for systemically transporting molecular drugs into the skin [120]. It provides a possible alternative to the traditional drug delivery methods such as oral administration or hypodermic injection by overcoming the various limitations including allergic reactions, risks of infection, needle phobia, bleeding, and psychological stress to patients [121-125] and providing direct absorption via microcirculation with less limitation on pH requirements, susceptibility to enzymes, and complicated metabolism [126-129]. However, as the natural permeation of the foreign molecules through the skin is extremely slow [130-131], advanced transdermal strategies with maximized drug flux but minimal invasion are necessary.

Microneedles (MNs) are the best fit for these ambivalent requirements: as a minimally invasive method with negligible pain, the MNs create microchannels through which drugs can travel into the skin [132]. Moreover, MNs can easily be combined with the iontophoresis mechanism and effectively deliver charged drug molecules [133-134]. Biocompatible metals like stainless steel or titanium are used for MNs, with sufficient mechanical strength and excellent electric conductivity to apply an electric field to charged drug molecules [133, 135-139]. Despite the advantages, these metals can cause allergic reactions, local anaphylaxis inflammation, or pigmentation by releasing toxin ions if the MNs got broken inside the skin [140-141].

The Mg-based materials are good candidates to overcome the challenges mentioned above, especially the danger of broken MNs, and have already been actively studied for their safety in the fields of orthopedics, dental, and cardiology [13, 142]. As metallic materials, they have sufficient strength to penetrate the skin and can be used as electrodes. Nevertheless, they have not been significantly considered as MN electrodes for iontophoresis due to the severe corrosion

generating hydrogen gas in vivo, far different from conventional electrochemical electrode materials.

Herein, we report the application of Mg as electrochemical electrodes for iontophoretic MNs: the H_2 generation behavior on both Mg anode and Mg cathode (**Figure 19**) was thoroughly analyzed as a function of applied voltage together with the dye migration in the porcine skin model to determine the optimum potential range for enhanced TDD. These investigations are essential to overcome the difficulties arising from the application of electrochemically active Mg to electrodes: the efficiency of drug delivery is proportional to the strength of the electric field, but high voltage can trigger cell or skin damage [143-144]. Also, vigorous H_2 generation, so the optimization for precise control of electric potential is required.

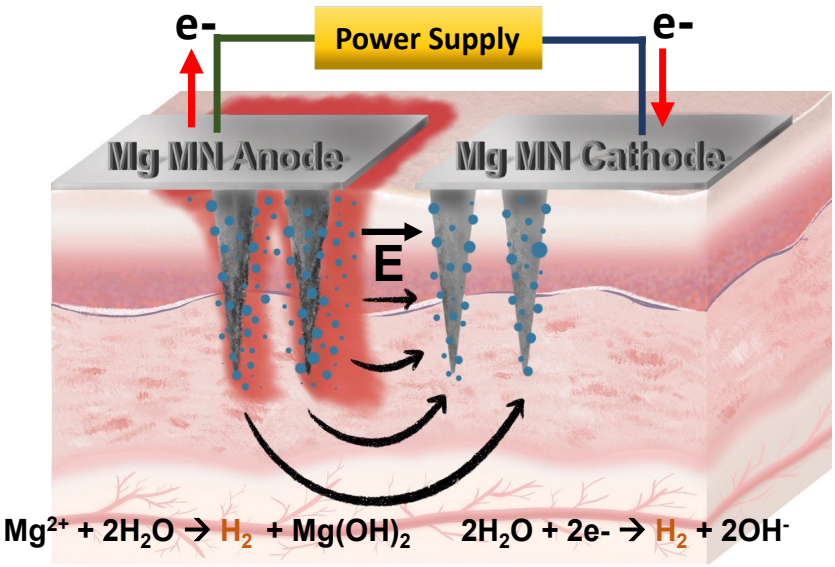

Figure 19. Schematic illustration of the iontophoretic Mg microneedle electrodes for diffusion of drug molecules into the skin.

4.2 Experimental Procedures

4.2.1 Fabrication of the Mg MN

The Mg plate was polished up to 2000 grit and cleaned in an ultrasonic bath with absolute ethanol. The polished Mg plate was cut into 6 × 2 MN arrays using a fiber nanosecond laser (Biolino series, Laservall, China), and each needle had a length and width of 1000 μm and 500 μm, respectively. The laser system was set up with a pulse duration of 8 ns at a central wavelength of 1070 nm. The laser power was 20 W, the spot diameter was 60 μm, and the scanning speed was 1000 mm s^{-1}. Each needle was erected by pushing the straight pin and sterilized in an ultrasonic bath with absolute ethanol and acetone, respectively, before use.

4.2.2 Penetration test of the Mg MN

Porcine skin was used for the penetration and dye permeation tests of the Mg MN. Porcine samples were acquired from a local butcher shop and immediately stored at – 80 °C until further analysis. Before the experiment, the porcine sample was thawed to room temperature by immersing in a 1 × PBS (pH 7.4, Welgene) to prevent surface drying. Then, the porcine sample was thoroughly cleaned with deionized water to remove subcutaneous fat, and cut into 2 × 2 cm slabs with a thickness of 3 ± 0.2 mm. PDMS (Sylgard 184, Dow Corning, USA) resin was used as a support structure for the Mg MNs on the porcine sample. First, the PDMS resin was mixed with a curing agent at a ratio of 10:1 (v/v). Air bubbles trapped in the PDMS were removed using vacuum equipment, and the mixture was cured at 70 °C overnight. The red fluorescent dye solution was prepared by dissolving Rhodamine B (0.2 mg, 0.44 mM) (Sigma Aldrich, USA) in ethanol. The Mg MN was dipped into the dye solution and placed on the porcine sample at a distance of 3 mm. Then, the coated Mg MNs were pushed by a finger for a while to enable penetration into the porcine sample, followed by pressing with PDMS to secure it for 1 h. The porcine skin marked by the Mg MN was verified with a digital camera, and the depth of a single puncture was investigated using a 3D microscope (OLS5000, Olympus, Japan).

4.2.3 Potential measurement of the Mg and Mg alloys electrodes

Mg rectangular electrodes were used for the potential level measurement, H_2 generation

test, and H_2O_2 generation test. The electrodes were fabricated by cutting the polished plate in a 1.5 × 1 cm rectangular shape using a fiber nanosecond laser and sterilized in an ultrasonic bath with absolute ethanol and acetone, respectively. The potential of the electrodes was measured using a potentiostat (VersaSTAT 3, AMETEK, USA) with the Mg electrode, Ag/AgCl, and Pt plate as the working electrode, reference electrode, and counter electrode, respectively, in 1 × PBS solution. Then, the working electrode was connected to the DC power supply (RDP-305, SMART, Korea) as an anode or cathode. The potential of the Mg alloy electrodes was measured in the same manner.

4.2.4 H_2 generation test of the Mg and Mg alloys electrodes

The Mg rectangular electrodes were attached with long electrical lines, and the attaching part was thoroughly enveloped by a commercial epoxy resin. Then, the two electrodes were connected to the DC power supply as an anode and a cathode, respectively, and soaked in 1 × PBS solution. The system was covered with an upside downed funnel, and the H_2 generated during immersion of the Mg electrodes under applied voltage was collected in the column part of the funnel. The volume change was observed and converted to the amount of H_2 generated. The H_2 generation test of the Mg alloy electrodes was performed in the same manner.

4.2.5 H_2O_2 generation test of the Mg electrodes

Two Mg rectangular electrodes as the anode and cathode were connected to the DC power supply, and the voltage was applied to the electrodes in 1 × PBS solution for 1 h. The 50 μl working samples captured at certain times and the 50 μl H_2O_2 standard solutions to draw a linear curve of the H_2O_2 concentration were seeded into a 96-well black plate. Subsequently, 50 μl Mater Mix of the Fluorimetric Hydrogen Peroxide Assay Kit (Sigma Aldrich, USA) was added to each well and incubated for 10 min. Fluorescence was measured using a microplate reader (GloMax® Discover, PromegaTM, USA) with an excitation wavelength of 540 nm and an emission wavelength of 590 nm. The fluorescence intensity values were converted into the concentration of H_2O_2 generated.

4.2.6 Dye permeation test on the porcine skin

The porcine sample was coated by dropping the red dye solution of Rhodamine B (0.44 mM in ethanol). Two Mg MNs were placed on the drop-cast porcine sample at a distance 3 mm and connected to the DC power supply as an anode and a cathode. Then, the Mg MNs were manually pushed for a while to enable penetration into the porcine sample, followed by pressing with PDMS to secure it for 1 h under applied voltage. Then, the Mg MN-treated porcine skin was fixed with formaldehyde (4%) for 30 min, embedded in a frozen section compound (FSC 22 ® Clear, Leica) medium, and stored at −80 °C overnight. The frozen sample was then cut using a single edged knife to obtain cross-sectional images of the MN insertion site.

4.2.7 Area analysis for dye migration

Cross-sectional images of the porcine samples inserted with the Mg MNs were analyzed to quantify dye permeation during iontophoresis. Each image was uniformly cut at a certain area in the vicinity of the Mg MN anode, and the area of the dye distribution was analyzed by Image J software. The results are presented as the mean ± SD. Statistical analysis was performed using one-way (ANOVA) with Tukey's test using Origin software.

4.2.8 Mg MN Characterization

The Mg MNs after insertion into the porcine sample during the 1 h period of iontophoresis was washed with deionized water and dried. Subsequently, the Mg MN samples were coated with a thin layer of platinum prior to imaging. SEM (Inspect F 50, FEI Company, USA) images were captured at an acceleration voltage of 10 kV. Then, the elemental composition of the Mg MNs was analyzed using EDS (Octane Silicon Drift Detector, AMETEK EDAX, USA) attached to the SEM instrument.

4.3 Results and Discussion

4.3.1 Fabrication and penetration test of the Mg MN

The Mg MN electrodes were readily fabricated with a fiber nanosecond laser (**Figure 20a**). For successful transdermal drug delivery, the MNs should be able to penetrate at least 150μm into the skin [145]. However, as the average depth of skin penetration is only 10-30 % of the total needle length [146], the Mg MNs were designed with a length and width of 1000μm and 500μm respectively, in 6 × 2 arrays **(Figure 20b)**. To analyze the penetration behavior of the Mg MNs, they were tested with porcine skin samples. The Mg MNs were dipped into the dye solution (Rhodamine B, 0.44 mM) for visualization and inserted into the porcine skin. After removal of Mg MNs, the porcine sample showed microchannels marked with Rhodamine B after 1 hour (**Figure 20c**). The depth of a single puncture on the porcine skin was investigated with 3D microscopy (**Figure 20d** and **20e**). The indented mark was about 290 μm deep after 1 hour of the MN insertion (**Figure 20f**), which was about 30 % of the total MN length. So, it can be concluded that pure Mg MNs have sufficient strength to penetrate the skin and form microchannels for drug transport.

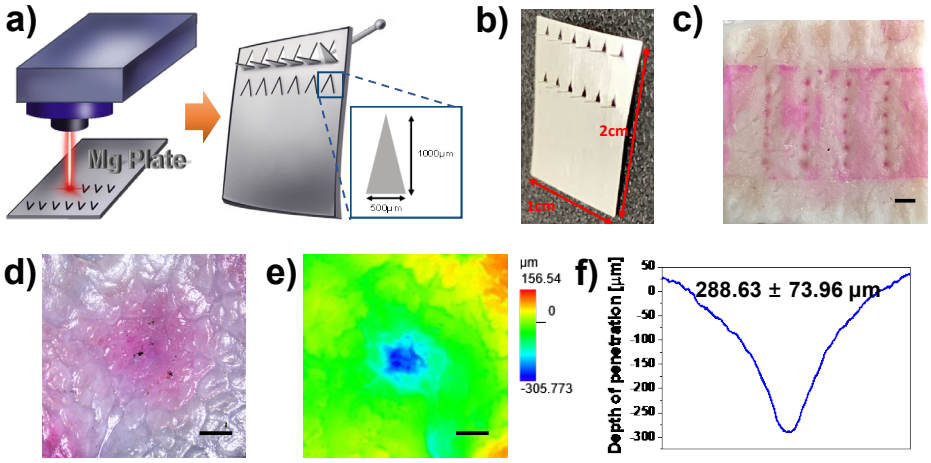

Figure 20. a) The fabrication process of the Mg microneedles, b) optical images of the 6 x 2 array of Mg microneedles, c) visualization of microchannel created by the Mg microneedles with Rhodamine B into the porcine samples (scale bar: 2 mm), d) close up image (scale bar: 200 μm), e) 3D depth microscopy profile image (scale bar: 200 μm) and f) the average depth of a single puncture on the porcine sample stained by Rhodamine B after 1 h of the Mg microneedle insertion. (Mean ± SD, n = 10)

4.3.2 Establishment of applied potential range

In the iontophoresis application, as Mg MN electrodes act as anode and cathode or alternately, it is necessary to analyze electrochemical reactions such as Mg corrosion and hydrogen evolution at each electrode according to the applied voltage. As ease of use is one of the main advantages of MNs, an electrochemical study was conducted assuming a direct current (DC) voltage of an alkaline battery. **Figure 21a** shows the potential levels of each Mg electrode when voltage was applied. Compared to the OCP of pure Mg (−1.58 V in PBS solution), the potential of the Mg anodes slightly moved in the positive direction, while the levels of the Mg cathodes significantly moved in the negative direction based on the OCP level as the applied voltage increased. The potential difference between anode and cathode was almost identical to the applied voltage. The direction to which the potential moved was influenced by overpotential, which increased with increasing current density according to the Tafel equation. (η: overpotential, A: Tafel slope, i: current density, and i_0: exchange current density), as the following equation; $\eta = \pm A \times log\ (i/i_0)$. Hence, the greater the voltage applied, the more vigorous became the chemical reaction on the Mg electrodes.

The H_2 generated on the Mg electrodes was measured as a function of applied voltage. The H_2 generation increases as the applied voltage increases (**Figure 21b**). Initially, H_2 was rapidly generated on the surface of Mg electrodes, and the amount gradually decreased over time (**Figure 21c**) [76, 99-100, 147]. The H_2 amount after 30 min, 1 h, and 2 h was rearranged as a function of applied voltage for the establishment of the optimum potential range (**Figure 21d**). At an applied voltage of 1.2 V or higher, H_2 was very rapidly generated, and the electrodes got completely dissolved between 1 h and 2 h and further measurement was impossible. In the applied voltage range up to 1.0 V, H_2 generation for 30min and 1h slowly increased with the increment of the applied voltage. So, up to 1.0 V, it can be expected that the H_2 generation would not be too vigorous to prevent the transport of drugs along the surface of Mg MNs or microchannel around MNs and their diffusion in the tissue.

Practically, alloys are more commonly used than pure Mg because of their superior corrosion resistance and strength. Mg-Ca-Zn alloys have been actively studied as biomaterials due to their excellent biocompatible and biodegradable properties, in addition to their controlled

corrosion rate and strength [9-11]. As an example study, Mg-0.05Ca-1Zn was selected and its potential levels and amount of H_2 were measured in the same way as pure Mg under the applied voltage. The potential levels of the Mg-0.05Ca-1Zn electrodes shifted in a similar manner to pure Mg electrodes (**Figure 21f**). The H_2 generation on Mg-0.05Ca-1Zn electrodes increased as the applied voltage increased (**Figure 21g**), but it is noteworthy that the amount of H_2 with 1.2 V was almost identical to that on pure Mg with 1.0 V and did not show abrupt increment up to 1.4 V (**Figure 21h**). So, it can be inferred that Mg-0.05Ca-1Zn alloy MNs may show identical or superior performance to Mg MNs up to 1.2 V and even be used at 1.4 V. By far, we assumed H_2 evolution as an obstacle to drug delivery. However, adequate H_2 generation could physically drive the drugs into the skin more effectively [33]. Therefore, a suitable voltage range should be decided by comprehensively considering the driving effect of the applied voltage and the accelerating or hindering effect of H_2 generation on the drug molecules.

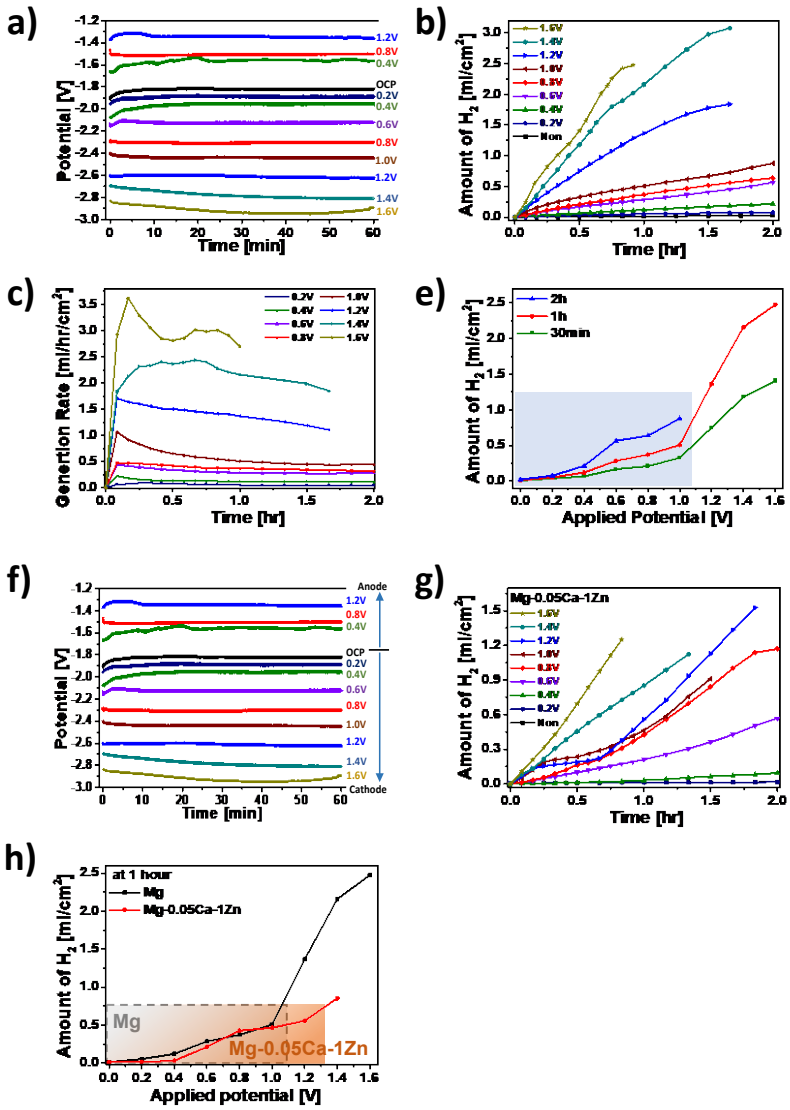

Figure 21. Fundamental study of Mg electrodes a) the potential of each pure Mg electrode under the applied potential (vs. Ag/AgCl), b) H_2 generation and c) H_2 generation rate curves of the pure Mg electrodes under the applied potential, d) the potential window of the pure Mg electrodes based on the amount of H_2 generation at fixed times, f) the potential and g) H_2 generation curve of Mg-0.05Ca-1Zn electrodes under the applied potential (vs. Ag/AgCl), h) the potential window change of the Mg based metals based on the amount of H_2 generation at 1 h.

4.3.3 Dye permeation test on the porcine skin

To test the efficacy of Mg electrodes for iontophoresis and determine the optimum voltage range, the dye permeation test was performed with anodic and cathodic Mg MNs using Rhodamine B solution, instead of actual drugs [146, 148-150]. The solution was loaded by a drop-casting method on the porcine skin surface. The Mg MN electrodes were attached to the dye-loaded porcine sample, and voltage was applied for 1h (**Figure 22a**). The resultant iontophoresis effect was clearly visible with the naked eyes (**Figure 22b**): in control samples (0 V), the dye moved into the skin only by diffusion, whereas the dye migrated deeper and farther with applied voltage. Previously, iontophoresis studies have been conducted at a current density of 0.2 – 0.5mA cm^{-2} on MN electrodes to avoid human skin damage [134, 136, 151-153]. In this study, the application of 0.8 V corresponds to the above-mentioned range as a current density of 0.43 mA cm^{-2} without notable change by time (**Figure 22c**).

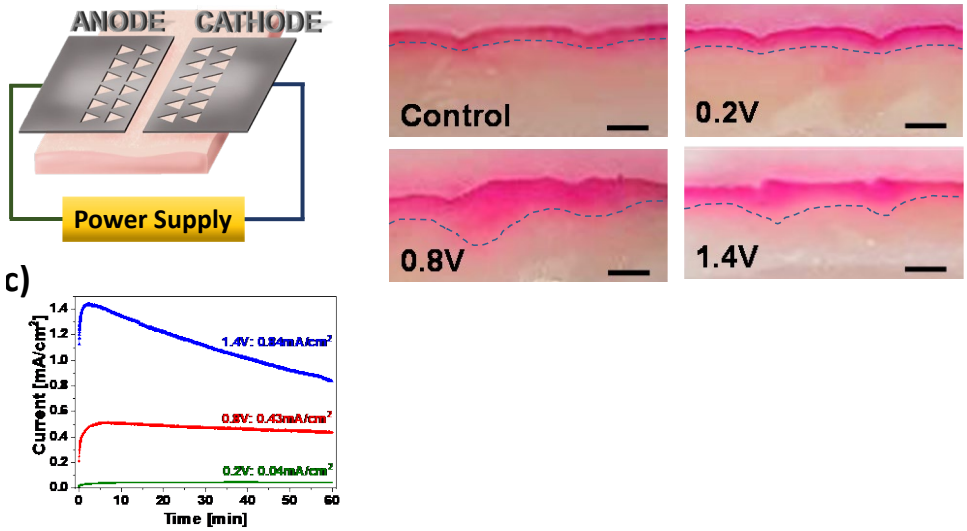

Figure 22 a) Schematic illustration of experimental set up of the dye migration test during iontophoretic investigations, b) optical cross-sections images of the porcine samples after 1 h of insertion under the applied potential (scale bar: 1mm), c) current change curve for 1 h of Mg microneedle insertion into the porcine skin under the applied potential.

Statistical analysis of the dyed area was conducted due to the roughness and irregularity of the porcine skin surface. In the optical cross-section images near the Mg MN anode, the dyed region was extracted and quantified using ImageJ software. The process is described in **Figure 23a** in detail. The dyed areas under applied voltage were larger than those of the control group only depending on the intrinsic diffusion without voltage (**Figure 23b**). The dye was delivered to a wider area with the increment of applied voltage, but the dyed area decreased at 1.4 V. It can be concluded that the dye-driving effect by applied voltage was dominant within a mild H_2 generation range (~ 0.5 ml cm^{-2} for 1h), but higher voltages (1.4 V ~) leading to active H_2 generation (more than 2 ml cm^{-2} for 1h) interrupted dye migration rather than driving it farther during iontophoresis.

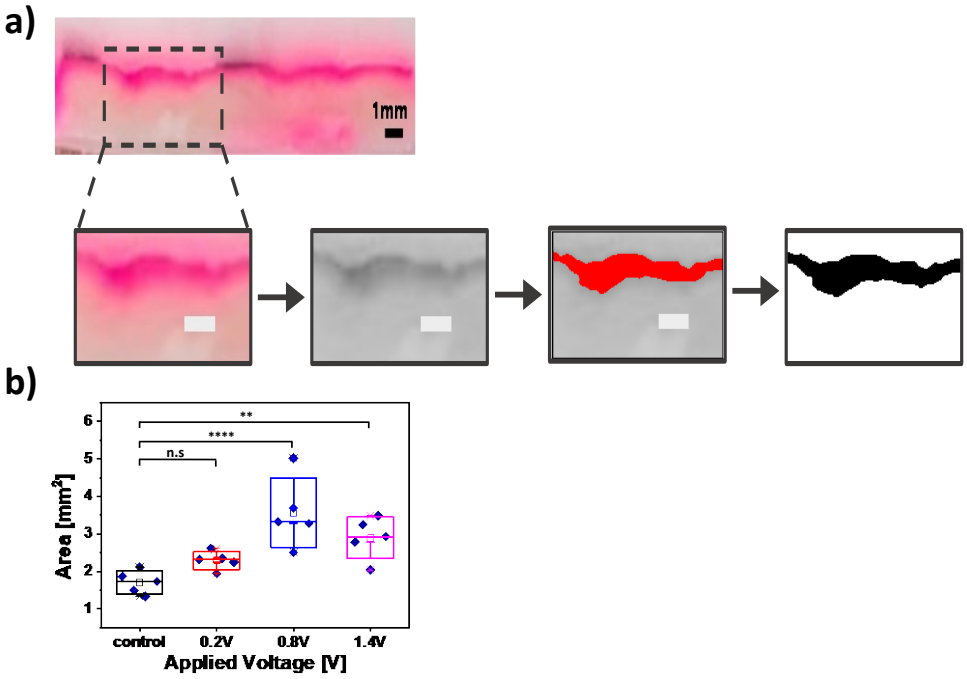

Figure 23. a) The area analysis process of dye migration in the porcine samples after 1 h of Mg microneedle insertion under the applied potential. b) area change curve of dye migration after 1 h of insertion under the applied potential. (One-way ANOVA with Turkey's test Mean ± SD n = 5, n.s = no significant *p<0.05, **p<0.01, ***p<0.001, ****p<0.0001)

4.3.4 Characterization of the Mg MN electrodes

The SEM images show a considerable difference between the anodic and cathodic Mg MN electrodes after they had been attached to the porcine sample at 0.8 V for 1 h. While the needle tip of the anode got corroded and disappeared (**Figure 24a i**), the shape of the cathode was almost retained during the iontophoresis (**Figure 24a ii**). The EDS results showed that the amount of oxygen was much higher in the anode (**Table 3a**). The SEM images in **Figure 24b** show the corroded Mg MN anodes with different applied voltages. As the applied voltage increased, the corrosion became severer and a more amount of oxygen was detected (**Table 3b**). Specifically, only the tip of the needle disappeared at 0.8 V showing the maximum dyed area, whereas, at 1.4 V, the needle almost disappeared during the 1h period. As previously discussed, dye migration decreased at 1.4 V, which was attributed to the abrupt increase of the H_2 generation during iontophoresis. Considering the anode image at 1.4 V (**Figure 24b**), it can also be inferred that it became harder as time elapsed for the dye diffusion into the porcine skin along the anodic MNs which got corroded and gradually disappeared.

Like other iontophoresis studies [151, 153], Rhodamine B dye was used to conveniently visualize the electric field effect in this study. However, many the drug molecules have a negative charge [154-155], then they would go to the anodes from the cathode during iontophoresis. So, the H_2 generation at each Mg electrode was separately measured as shown in **Figure 24c**. As the applied voltage increased, the H_2 generation at the cathode increased, but much less than that at the anode. For example, the amount of H_2 generated on the cathode at 1.6 V was less than that on the anode at 1.2 V. This implies that negatively charged drugs can be delivered using the Mg MNs with applied voltage up to 1.6 V, due to the slow H_2 generation rate and cathodic MNs maintaining their shape for 1 h. H_2O_2 was also generated by the Mg corrosion (**Figure 24d**). With the increment of applied voltage, i.e., increased H_2 generation, the amount of H_2O_2 decreased, and this seems to be the pH change by Mg ions (**Figure 24e**) [24, 156].

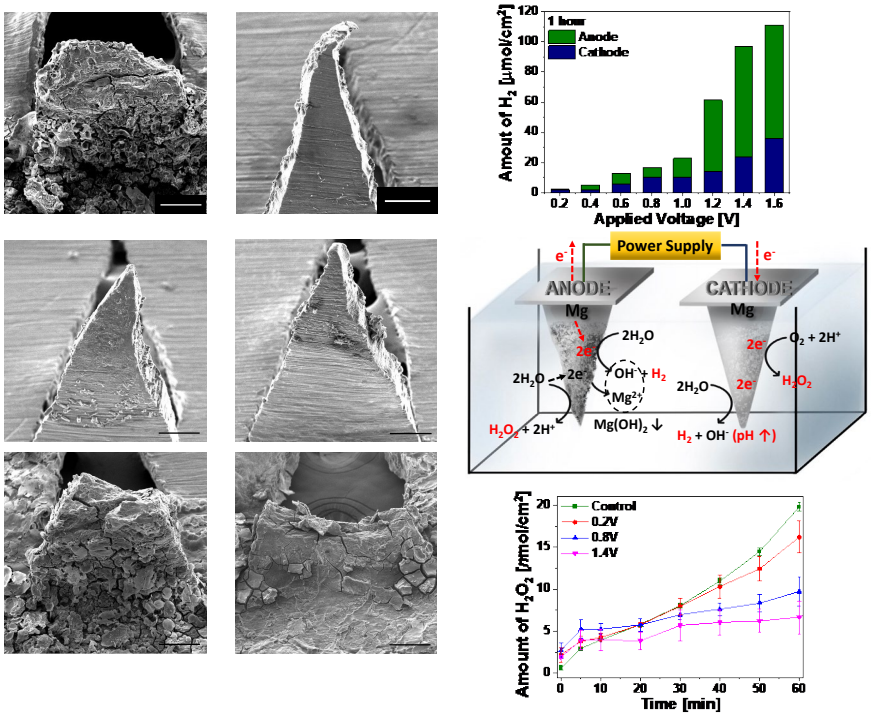

Figure 24 a) SEM images of i) the Mg microneedle anode and ii) the Mg microneedle cathode after 1 h of insertion into the porcine sample under 0.8 V (scale bar: 100 μm), b) SEM images of the Mg microneedle anodes after 1 h of insertion into the porcine samples under the applied potential (scale bar: 100 μm), c) H_2 generation curve on each pure Mg electrode under the applied potential for 1 h, d) schematic illustration of the H_2 and H_2O_2 generation mechanism on each pure Mg electrode, e) total H_2O_2 generation on the pure Mg electrodes under the applied potential for 1 h.

Table 3. Elemental composition by EDS of a) the Mg microneedle (MN) electrodes after 1 h of insertion into the porcine sample at 0.8 V, and b) the Mg MN anodes after 1 h of insertion into the porcine samples under the applied potential.

a)

Element	Anode		Cathode	
	Wt%	At%	Wt%	At%
C	13.72	20.51	31.09	46.12
O	45.14	50.66	8.89	9.9
Mg	33.23	24.54	60.01	43.97
Cl	4.09	2.07		

b)

Element	Wt%			
	Control	0.2V	0.8V	1.4V
C	46.58	26.62	13.72	7.65
O	11.68	16.57	45.14	49.07
Mg	41.75	56.8	33.23	40.85
Cl			4.09	2.43

4.4 Conclusion

Biocompatible and biodegradable Mg electrodes were studied for enhancing TDD by combining MN technology and iontophoresis. The Mg MNs formed microchannels deep enough for drug delivery into the skin. Then, during iontophoresis, the potential levels of Mg and Mg-based alloy were measured and their optimum voltage ranges were established based on the amount of H_2 generation. The dye permeation test on the porcine skin samples obviously proved the efficacy of the Mg electrodes for iontophoresis. The dye migrated farther as the applied voltage increased, but the dye transport was hindered by excessive H_2 generation and MN corrosion at a high applied voltage, 1.4 V. By analyzing the H_2 generation and MN corrosion at each electrode, they clearly indicate that the Mg MNs are adequate for iontophoretic TDD regardless of the polarity of the drugs. In addition, it is expected that this study would serve as an opportunity to further expand the application of biodegradable metals even to various electrochemical applications.

Chapter 5. Conclusion

Mg is used in various medical engineering fields such as orthopedics and dentistry due to its excellent mechanical properties, excellent biocompatibility, and biodegradable properties. Despite these advantages, the most limiting reason for the use of Mg is its aggressive corrosion rate. In particular, the dynamic corrosion process in the initial corrosion stage plays a decisive role in cell attachment and cell-surface bonding, and determines the success of implant materials. Therefore, it is very important to understand the corrosion mechanism of Mg. Mg and Mg-based alloys generate corrosion products such as H_2, ROS and various oxides during the corrosion process. Therefore, through understanding the corrosion mechanism of Mg and its alloys, we tried to control corrosion products and expand their use in the field of biomedical engineering.

First, we developed a biodegradable hybrid material that can generate ROS using a simple coating layer of biodegradable metals Mg and Zn without external stimulation. A galvanic couple of the two coating layers accelerated the corrosion of Mg and generated more ROS than single metal layer. The ROS generation tendency was closely analyzed through the long-term immersion test. Therefore, Mg/Zn/PLLA hybrid materials are good candidates for biodegradable hybrid stent materials with ROS functionalization to suppress the risk of in-stent restenosis

Second, the ROS generation mechanism of Mg and Mg-based alloys was studied. The corrosion rate of metal was proportional to the amount of H_2 generated, but not related to ROS. As a result of measuring ROS by supplying a constant current to control the inherent characteristics of the alloy, it was found that the supply of electrons contributes to the generation of ROS to some extent, but the inherent surface properties of the alloy are a more important factor. In addition, this was proved through the oxide film model tests. Through this, research using ROS generation based on Mg materials will be able to expand not only to the field of biomedical engineering but also to various fields such as catalysts and the environment.

Third, biocompatible and biodegradable Mg electrodes were studied for enhancing TDD by combining MN technology and iontophoresis. The Mg MNs formed microchannels deep enough for drug delivery into the skin. Then, during iontophoresis, the potential levels of Mg and Mg-based alloys were measured and their optimum voltage ranges were established based on the

amount of H_2 generation. The dye permeation test on the porcine skin samples obviously proved the efficacy of the Mg electrodes for iontophoresis. By analyzing the H_2 generation and MN corrosion at each electrode, they clearly indicate that the Mg MNs are adequate for iontophoretic TDD regardless of the polarity of the drugs. In addition, it is expected that this study would serve as an opportunity to further expand the application of biodegradable metals even to various electrochemical applications.

References

[1] Bauer, S.; Schmuki, P.; von der Mark, K.; Park, J., Engineering biocompatible implant surfaces: Part I: Materials and surfaces. *Progress in Materials Science* **2013,** *58* (3), 261-326.

[2] Seetharaman, S.; Jayalakshmi, S.; Arvind Singh, R.; Gupta, M., The Potential of Magnesium-Based Materials for Engineering and Biomedical Applications. *Journal of the Indian Institute of Science* **2022,** *102* (1), 421-437.

[3] Ghosh, S.; Sanghavi, S.; Sancheti, P., 6 - Metallic biomaterial for bone support and replacement. In *Fundamental Biomaterials: Metals*, Balakrishnan, P.; M S, S.; Thomas, S., Eds. Woodhead Publishing: 2018; pp 139-165.

[4] Staiger, M. P.; Pietak, A. M.; Huadmai, J.; Dias, G., Magnesium and its alloys as orthopedic biomaterials: A review. *Biomaterials* **2006,** *27* (9), 1728-1734.

[5] Zheng, Y. F.; Gu, X. N.; Witte, F., Biodegradable metals. *Materials Science and Engineering: R: Reports* **2014,** *77*, 1-34.

[6] Witte, F.; Eliezer, A., Biodegradable Metals. In *Degradation of Implant Materials*, Eliaz, N., Ed. Springer New York: New York, NY, 2012; pp 93-109.

[7] Dorozhkin, S. V., Calcium orthophosphate coatings on magnesium and its biodegradable alloys. *Acta biomaterialia* **2014,** *10* (7), 2919-2934.

[8] Uddin, M. S.; Hall, C.; Murphy, P., Surface treatments for controlling corrosion rate of biodegradable Mg and Mg-based alloy implants. *Science and technology of advanced materials* **2015,** *16* (5), 053501.

[9] Pan, Y.; He, S.; Wang, D.; Huang, D.; Zheng, T.; Wang, S.; Dong, P.; Chen, C., In vitro degradation and electrochemical corrosion evaluations of microarc oxidized pure Mg, Mg–Ca and Mg–Ca–Zn alloys for biomedical applications. *Materials Science and Engineering: C* **2015,** *47*, 85-96.

[10] Gong, C.; He, X.; Yan, X., Corrosion behavior of Mg–Ca–Zn alloys with high Zn content. *Journal of Physics and Chemistry of Solids* **2021,** *152*, 109952.

[11] Cha, P.-R.; Han, H.-S.; Yang, G.-F.; Kim, Y.-C.; Hong, K.-H.; Lee, S.-C.; Jung, J.-Y.; Ahn, J.-P.; Kim, Y.-Y.; Cho, S.-Y.; Byun, J. Y.; Lee, K.-S.; Yang, S.-J.; Seok, H.-K., Biodegradability

engineering of biodegradable Mg alloys: Tailoring the electrochemical properties and microstructure of constituent phases. *Scientific Reports* **2013,** *3* (1), 2367.

[12] Tsakiris, V.; Tardei, C.; Clicinschi, F. M., Biodegradable Mg alloys for orthopedic implants – A review. *Journal of Magnesium and Alloys* **2021,** *9* (6), 1884-1905.

[13] Li, X.; Zhang, W.; Lin, W.; Qiu, H.; Qi, Y.; Ma, X.; Qi, H.; He, Y.; Zhang, H.; Qian, J.; Zhang, G.; Gao, R.; Zhang, D.; Ding, J., Long-Term Efficacy of Biodegradable Metal–Polymer Composite Stents After the First and the Second Implantations into Porcine Coronary Arteries. *ACS Applied Materials & Interfaces* **2020,** *12* (13), 15703-15715.

[14] Kim, S.-Y.; Kim, Y.-K.; Kim, K.-S.; Lee, K.-B.; Lee, M.-H., Enhancement of bone formation on LBL-coated Mg alloy depending on the different concentration of BMP-2. *Colloids and Surfaces B: Biointerfaces* **2019,** *173*, 437-446.

[15] Sadeghabadi, A.; Sadrnezhaad, S. K.; Asefnejad, A.; Hassanzadeh Nemati, N., Fabrication and evaluation of bioresorbable scaffolds for interventional cardiology application with sufficient drug release. *Iranian journal of basic medical sciences* **2022,** *25* (3), 372-382.

[16] Zander, D.; Zumdick, N. A., Influence of Ca and Zn on the microstructure and corrosion of biodegradable Mg–Ca–Zn alloys. *Corrosion Science* **2015,** *93*, 222-233.

[17] Cho, S. Y.; Chae, S.-W.; Choi, K. W.; Seok, H. K.; Kim, Y. C.; Jung, J. Y.; Yang, S. J.; Kwon, G. J.; Kim, J. T.; Assad, M., Biocompatibility and strength retention of biodegradable Mg-Ca-Zn alloy bone implants. *Journal of Biomedical Materials Research Part B: Applied Biomaterials* **2013,** *101B* (2), 201-212.

[18] Jamel, M.; Jamel, M.; Lopez, H., Designing Advanced Biomedical Biodegradable Mg Alloys: A Review. *Metals* **2022,** *12*, 85.

[19] Cai, S.; Lei, T.; Li, N.; Feng, F., Effects of Zn on microstructure, mechanical properties and corrosion behavior of Mg–Zn alloys. *Materials Science and Engineering: C* **2012,** *32* (8), 2570-2577.

[20] Ben-Hamu, G.; Eliezer, D., Corrosion behavior of wrought Mg–6%Zn–1%Mn–XSi–YCa alloy. *Materials and Corrosion* **2013,** *64* (6), 516-521.

[21] Ascencio, M.; Pekguleryuz, M.; Omanovic, S., An investigation of the corrosion mechanisms of WE43Mg alloy in a modified simulated body fluid solution: The effect of

electrolyte renewal. *Corrosion Science* **2015,** *91*, 297-310.

[22] Shi, Z.; Atrens, A., An innovative specimen configuration for the study of Mg corrosion. *Corrosion Science* **2011,** *53* (1), 226-246.

[23] Park, J.; Du, P.; Jeon, J.-K.; Jang, G. H.; Hwang, M. P.; Han, H.-S.; Park, K.; Lee, K. H.; Lee, J.-W.; Jeon, H.; Kim, Y.-C.; Park, J. W.; Seok, H.-K.; Ok, M.-R., Magnesium Corrosion Triggered Spontaneous Generation of H2O2 on Oxidized Titanium for Promoting Angiogenesis. *Angewandte Chemie International Edition* **2015,** *54* (49), 14753-14757.

[24] Jeong, G.; Hwang, H. W.; Chae, M.; Hong, S. H.; Park, J.; Han, Y.; Jeon, H.; Kim, Y.-C.; Kang, S.-K.; Jang, H. W.; Sun, J.-Y.; Ok, M.-R., Development of Organic/Inorganic Hybrid Materials for Fully Degradable Reactive Oxygen Species-Releasing Stents for Antirestenosis. *Langmuir* **2022,** *38* (26), 8003-8011.

[25] Krumova, K.; Cosa, G., Chapter 1 Overview of Reactive Oxygen Species. In *Singlet Oxygen: Applications in Biosciences and Nanosciences, Volume 1*, The Royal Society of Chemistry: 2016; Vol. 1, pp 1-21.

[26] Xin, Y.; Hu, T.; Chu, P., Influence of Test Solutions on In Vitro Studies of Biomedical Magnesium Alloys. *Journal of The Electrochemical Society - J ELECTROCHEM SOC* **2010,** *157*.

[27] Wu, G.; Ibrahim, J. M.; Chu, P. K., Surface design of biodegradable magnesium alloys — A review. *Surface and Coatings Technology* **2013,** *233*, 2-12.

[28] Xin, Y.; Hu, T.; Chu, P. K., In vitro studies of biomedical magnesium alloys in a simulated physiological environment: a review. *Acta biomaterialia* **2011,** *7* (4), 1452-9.

[29] Noviana, D.; Paramitha, D.; Ulum, M. F.; Hermawan, H., The effect of hydrogen gas evolution of magnesium implant on the postimplantation mortality of rats. *Journal of Orthopaedic Translation* **2016,** *5*, 9-15.

[30] Yang, Y.; Scenini, F.; Curioni, M., A study on magnesium corrosion by real-time imaging and electrochemical methods: relationship between local processes and hydrogen evolution. *Electrochimica Acta* **2016,** *198*, 174-184.

[31] Chen, K.; Dai, J.; Zhang, X., Improvement of corrosion resistance of magnesium alloys for biomedical applications. *Corrosion Reviews* **2015,** *33* (3-4), 101-117.

[32] Xu, D.; Han, E.-h.; Xu, Y., Effect of long-period stacking ordered phase on microstructure, mechanical property and corrosion resistance of Mg alloys: A review. *Progress in Natural Science: Materials International* **2016,** *26* (2), 117-128.

[33] Lopez-Ramirez, M. A.; Soto, F.; Wang, C.; Rueda, R.; Shukla, S.; Silva-Lopez, C.; Kupor, D.; McBride, D. A.; Pokorski, J. K.; Nourhani, A.; Steinmetz, N. F.; Shah, N. J.; Wang, J., Built-In Active Microneedle Patch with Enhanced Autonomous Drug Delivery. *Advanced Materials* **2020,** *32* (1), 1905740.

[34] Liu, L.; Wu, Y.; Ye, J.; Fu, Q.; Su, L.; Wu, Z.; Feng, J.; Chen, Z.; Song, J., Synthesis of magnesium nanoparticle for NIR-II-photoacoustic-imaging-guided synergistic burst-like and H2 cancer therapy. *Chem* **2022**.

[35] Li, Y.; Zhang, W.; Niu, J.; Chen, Y., Mechanism of Photogenerated Reactive Oxygen Species and Correlation with the Antibacterial Properties of Engineered Metal-Oxide Nanoparticles. *ACS Nano* **2012,** *6* (6), 5164-5173.

[36] Fu, S.; Zhu, C.; Song, J.; Du, D.; Lin, Y., Metal-Organic Framework-Derived Non-Precious Metal Nanocatalysts for Oxygen Reduction Reaction. *Advanced Energy Materials* **2017,** *7* (19), 1700363.

[37] Applerot, G.; Lipovsky, A.; Dror, R.; Perkas, N.; Nitzan, Y.; Lubart, R.; Gedanken, A., Enhanced Antibacterial Activity of Nanocrystalline ZnO Due to Increased ROS-Mediated Cell Injury. *Advanced Functional Materials* **2009,** *19* (6), 842-852.

[38] Leung, Y. H.; Ng, A. M. C.; Xu, X.; Shen, Z.; Gethings, L. A.; Wong, M. T.; Chan, C. M. N.; Guo, M. Y.; Ng, Y. H.; Djurišić, A. B.; Lee, P. K. H.; Chan, W. K.; Yu, L. H.; Phillips, D. L.; Ma, A. P. Y.; Leung, F. C. C., Mechanisms of Antibacterial Activity of MgO: Non-ROS Mediated Toxicity of MgO Nanoparticles Towards Escherichia coli. *Small* **2014,** *10* (6), 1171-1183.

[39] Bhattacharya, P.; Dey, A.; Neogi, S., An insight into the mechanism of antibacterial activity by magnesium oxide nanoparticles. *Journal of Materials Chemistry B* **2021,** *9* (26), 5329-5339.

[40] Karthik, K.; Dhanuskodi, S.; Gobinath, C.; Prabukumar, S.; Sivaramakrishnan, S., Fabrication of MgO nanostructures and its efficient photocatalytic, antibacterial and anticancer

performance. *Journal of Photochemistry and Photobiology B: Biology* **2019,** *190*, 8-20.

[41] Li, X.; Hong, X.; Yang, Y.; Zhao, J.; Diko, C. S.; Zhu, Y., Enhanced antibacterial activity of acid treated MgO nanoparticles on Escherichia coli. *RSC Advances* **2021,** *11* (60), 38202-38207.

[42] Zhang, Z.-Q.; Wang, L.; Zeng, M.-Q.; Zeng, R.-C.; Kannan, M. B.; Lin, C.-G.; Zheng, Y.-F., Biodegradation behavior of micro-arc oxidation coating on magnesium alloy-from a protein perspective. *Bioactive Materials* **2020,** *5* (2), 398-409.

[43] Li, X.; Feng, Y.; Li, H.; Zhang, Q., Effect of anionic groups on the antibacterial activity of magnesium oxide nanoparticles. *Colloids and Surfaces A: Physicochemical and Engineering Aspects* **2022,** *635*, 127978.

[44] Jiang, Z.; Wang, B.; Li, Y.; Chan, H. S.; Sun, H.; Wang, T.; Li, H.; Yuan, S.; Leung, M. K. H.; Lu, A.; Wong, P. K., Solar-light-driven rapid water disinfection by ultrathin magnesium titanate/carbon nitride hybrid photocatalyst: Band structure analysis and role of reactive oxygen species. *Applied Catalysis B: Environmental* **2019,** *257*, 117898.

[45] Wang, Y.; Xu, Y.; Dong, S.; Wang, P.; Chen, W.; Lu, Z.; Ye, D.; Pan, B.; Wu, D.; Vecitis, C. D.; Gao, G., Ultrasonic activation of inert poly(tetrafluoroethylene) enables piezocatalytic generation of reactive oxygen species. *Nature Communications* **2021,** *12* (1), 3508.

[46] Xu, J.; Zheng, X.; Feng, Z.; Lu, Z.; Zhang, Z.; Huang, W.; Li, Y.; Vuckovic, D.; Li, Y.; Dai, S.; Chen, G.; Wang, K.; Wang, H.; Chen, J. K.; Mitch, W.; Cui, Y., Organic wastewater treatment by a single-atom catalyst and electrolytically produced H2O2. *Nature Sustainability* **2021,** *4* (3), 233-241.

[47] Buccheri, D.; Piraino, D.; Andolina, G.; Cortese, B., Understanding and managing in-stent restenosis: a review of clinical data, from pathogenesis to treatment. *Journal of Thoracic Disease* **2016,** *8* (10), E1150-E1162.

[48] Shlofmitz, E.; Iantorno, M.; Waksman, R., Restenosis of Drug-Eluting Stents. *Circulation: Cardiovascular Interventions* **2019,** *12* (8), e007023.

[49] Park, S.-J.; Shim, W. H.; Ho, D. S.; Raizner, A. E.; Park, S.-W.; Hong, M.-K.; Lee, C. W.; Choi, D.; Jang, Y.; Lam, R.; Weissman, N. J.; Mintz, G. S., A Paclitaxel-Eluting Stent for the Prevention of Coronary Restenosis. *New England Journal of Medicine* **2003,** *348* (16), 1537-

1545.

[50] Giordano, A.; Romano, A., Inhibition of human in-stent restenosis: a molecular view. *Current Opinion in Pharmacology* **2011,** *11* (4), 372-377.

[51] Huang, J.; Song, G.-L.; Zhu, Y.; Zheng, D.; Wang, Z., The anodically polarized Mg surface products and accelerated hydrogen evolution. *Journal of Magnesium and Alloys* **2021**.

[52] Wang, J.; Xue, Y.; Liu, J.; Hu, M.; Zhang, H.; Ren, K.; Wang, Y.; Ji, J., Hierarchical Capillary Coating to Biofunctionlize Drug-Eluting Stent for Improving Endothelium Regeneration. *Research* **2020,** *2020*, 1458090.

[53] Yang, Y.; Gao, P.; Wang, J.; Tu, Q.; Bai, L.; Xiong, K.; Qiu, H.; Zhao, X.; Maitz, M. F.; Wang, H.; Li, X.; Zhao, Q.; Xiao, Y.; Huang, N.; Yang, Z., Endothelium-Mimicking Multifunctional Coating Modified Cardiovascular Stents via a Stepwise Metal-Catechol-(Amine) Surface Engineering Strategy. *Research* **2020,** *2020*, 9203906.

[54] Jinnouchi, H.; Torii, S.; Sakamoto, A.; Kolodgie, F. D.; Virmani, R.; Finn, A. V., Fully bioresorbable vascular scaffolds: lessons learned and future directions. *Nature Reviews Cardiology* **2019,** *16* (5), 286-304.

[55] Waksman, R., Promise and challenges of bioabsorbable stents. *Catheterization and Cardiovascular Interventions* **2007,** *70* (3), 407-414.

[56] Holmes, D. R.; Kereiakes, D. J.; Garg, S.; Serruys, P. W.; Dehmer, G. J.; Ellis, S. G.; Williams, D. O.; Kimura, T.; Moliterno, D. J., Stent Thrombosis. *Journal of the American College of Cardiology* **2010,** *56* (17), 1357-1365.

[57] Kirtane, A. J.; Stone, G. W., How to Minimize Stent Thrombosis. *Circulation* **2011,** *124* (11), 1283-1287.

[58] Zhu, Y.; Yang, K.; Cheng, R.; Xiang, Y.; Yuan, T.; Cheng, Y.; Sarmento, B.; Cui, W., The current status of biodegradable stent to treat benign luminal disease. *Materials Today* **2017,** *20* (9), 516-529.

[59] Hu, T.; Yang, C.; Lin, S.; Yu, Q.; Wang, G., Biodegradable stents for coronary artery disease treatment: Recent advances and future perspectives. *Materials Science and Engineering: C* **2018,** *91*, 163-178.

[60] Park, J.; Seo, H.; Hwang, H. W.; Choi, J.; Kim, K.; Jeong, G.; Kim, E. S.; Han, H.-S.;

Jung, Y.-W.; Seo, Y.; Jeon, H.; Seok, H.-K.; Kim, Y.-C.; Ok, M.-R., Interface Engineering of Fully Metallic Stents Enabling Controllable H2O2 Generation for Antirestenosis. *Langmuir* **2019,** *35* (10), 3634-3642.

[61] Bogdan, J.; Pławińska-Czarnak, J.; Zarzyńska, J., Nanoparticles of Titanium and Zinc Oxides as Novel Agents in Tumor Treatment: a Review. *Nanoscale Research Letters* **2017,** *12* (1), 225.

[62] Sivakumar, P.; Lee, M.; Kim, Y.-S.; Shim, M. S., Photo-triggered antibacterial and anticancer activities of zinc oxide nanoparticles. *Journal of Materials Chemistry B* **2018,** *6* (30), 4852-4871.

[63] Liu, Y.; Liu, X.; Zhang, Z.; Farrell, N.; Chen, D.; Zheng, Y., Comparative, real-time in situ monitoring of galvanic corrosion in Mg-Mg2Ca and Mg-MgZn2 couples in Hank's solution. *Corrosion Science* **2019,** *161*, 108185.

[64] Kolesnikov, A.; Kolek, M.; Dohmann, J. F.; Horsthemke, F.; Börner, M.; Bieker, P.; Winter, M.; Stan, M. C., Galvanic Corrosion of Lithium-Powder-Based Electrodes. *Advanced Energy Materials* **2020,** *10* (15), 2000017.

[65] Li, X.; Yang, S.; Dzakpasu, M.; Xu, S.; Ding, D.; Wang, G.; Chen, R.; Jin, P.; Wang, X. C., Galvanic corrosion of zero-valent iron to intensify Fe2+ generation for peroxymonosulfate activation. *Chemical Engineering Journal* **2021,** *417*, 128023.

[66] Park, J.; Han, H.-S.; Park, J.; Seo, H.; Edwards, J.; Kim, Y.-C.; Ok, M.-R.; Seok, H.-K.; Jeon, H., Corrosion behavior of biodegradable Mg-based alloys via femtosecond laser surface melting. *Applied Surface Science* **2018,** *448*, 424-434.

[67] Zhao, J.; Zhang, B.; Li, J.; Liu, Y.; Wang, W., Photo-enhanced oxidizability of tetrazolium salts and its impact on superoxide assaying. *Chemical Communications* **2016,** *52* (77), 11595-11598.

[68] Sutherland, M. W.; Learmonth, B. A., The Tetrazolium Dyes MTS and XTT Provide New Quantitative Assays for Superoxide and Superoxide Dismutase. *Free Radical Research* **1997,** *27* (3), 283-289.

[69] Han, H.-S.; Lee, S. H.; Kim, W.-J.; Jeon, H.; Seok, H.-K.; Ahn, J.-P.; Kim, Y.-C., Reduction of initial corrosion rate and improvement of cell adhesion through surface

modification of biodegradable Mg alloy. *Metals and Materials International* **2015,** *21* (1), 194-201.

[70] Lee, J.-W.; Han, H.-S.; Han, K.-J.; Park, J.; Jeon, H.; Ok, M.-R.; Seok, H.-K.; Ahn, J.-P.; Lee, K. E.; Lee, D.-H.; Yang, S.-J.; Cho, S.-Y.; Cha, P.-R.; Kwon, H.; Nam, T.-H.; Han, J. H. L.; Rho, H.-J.; Lee, K.-S.; Kim, Y.-C.; Mantovani, D., Long-term clinical study and multiscale analysis of in vivo biodegradation mechanism of Mg alloy. *Proceedings of the National Academy of Sciences* **2016,** *113* (3), 716-721.

[71] Park, J.; Jang, G. H.; Jung, Y. W.; Seo, H.; Han, H.-S.; Lee, J.; Seo, Y.; Jeon, H.; Ok, M.-R.; Cha, P.-R.; Seok, H.-K.; Lee, K. H.; Kim, Y.-C., Tailoring H2O2 generation kinetics with magnesium alloys for efficient disinfection on titanium surface. *Scientific Reports* **2020,** *10* (1), 6536.

[72] Deshpande, K. B., Experimental investigation of galvanic corrosion: Comparison between SVET and immersion techniques. *Corrosion Science* **2010,** *52* (9), 2819-2826.

[73] Miracle, D. B.; Donaldson, S. L.; Henry, S. D.; Moosbrugger, C.; Anton, G. J.; Sanders, B. R.; Hrivnak, N.; Terman, C.; Kinson, J.; Muldoon, K., *ASM handbook*. ASM international Materials Park, OH: 2001; Vol. 21.

[74] Bard, A., *Standard potentials in aqueous solution*. Routledge: 2017.

[75] Ng, W. F.; Chiu, K. Y.; Cheng, F. T., Effect of pH on the in vitro corrosion rate of magnesium degradable implant material. *Materials Science and Engineering: C* **2010,** *30* (6), 898-903.

[76] Maltseva, A.; Shkirskiy, V.; Lefèvre, G.; Volovitch, P., Effect of pH on Mg(OH)2 film evolution on corroding Mg by in situ kinetic Raman mapping (KRM). *Corrosion Science* **2019,** *153*, 272-282.

[77] Jiang, Q.; Yang, L.; Hou, B., The Effect of Deep Cryogenic Treatment on the Corrosion Behavior of Mg-7Y-1.5Nd Magnesium Alloy. *Metals* **2017,** *7* (10), 427.

[78] Liu, J.; Song, Y.; Chen, J.; Chen, P.; Shan, D.; Han, E.-H., The Special Role of Anodic Second Phases in the Micro-galvanic Corrosion of EW75 Mg Alloy. *Electrochimica Acta* **2016,** *189*, 190-195.

[79] Liew, Y.; Örnek, C.; Pan, J.; Thierry, D.; Wijesinghe, S.; Blackwood, D. J., Towards

understanding micro-galvanic activities in localised corrosion of AA2099 aluminium alloy. *Electrochimica Acta* **2021,** *392*, 139005.

[80] Feng, B.; Liu, G.; Yang, P.; Huang, S.; Qi, D.; Chen, P.; Wang, C.; Du, J.; Zhang, S.; Liu, J., Different role of second phase in the micro-galvanic corrosion of WE43 Mg alloy in NaCl and Na2SO4 solution. *Journal of Magnesium and Alloys* **2022,** *10* (6), 1598-1608.

[81] Kim, J.; Gilbert, J. L., In vitro cytotoxicity of galvanically coupled magnesium-titanium particles on human osteosarcoma SAOS2 cells: A potential cancer therapy. *Journal of Biomedical Materials Research Part B: Applied Biomaterials* **2019,** *107* (1), 178-189.

[82] Yang, N.; Gong, F.; Liu, B.; Hao, Y.; Chao, Y.; Lei, H.; Yang, X.; Gong, Y.; Wang, X.; Liu, Z.; Cheng, L., Magnesium galvanic cells produce hydrogen and modulate the tumor microenvironment to inhibit cancer growth. *Nature Communications* **2022,** *13* (1), 2336.

[83] Ho, C.-Y., Hydrolytic reaction of waste aluminum foils for high efficiency of hydrogen generation. *International Journal of Hydrogen Energy* **2017,** *42* (31), 19622-19628.

[84] Deng, M.; Wang, L.; Höche, D.; Lamaka, S. V.; Wang, C.; Snihirova, D.; Jin, Y.; Zhang, Y.; Zheludkevich, M. L., Approaching “stainless magnesium” by Ca micro-alloying. *Materials Horizons* **2021,** *8* (2), 589-596.

[85] Peng, H.; Wang, W.; Jiang, H.; Zan, R.; Sun, Y.; Yu, S.; Ni, J.; Wang, W.; Wang, T.; Wang, J.; Zhang, X., Effect of Galvanic Corrosion on the Degradability of Biomedical Magnesium. *Frontiers in Materials* **2021,** *8*.

[86] Wang, C.; Mei, D.; Wiese, G.; Wang, L.; Deng, M.; Lamaka, S. V.; Zheludkevich, M. L., High rate oxygen reduction reaction during corrosion of ultra-high-purity magnesium. *npj Materials Degradation* **2020,** *4* (1), 42.

[87] Stratmann, M.; Müller, J., The mechanism of the oxygen reduction on rust-covered metal substrates. *Corrosion Science* **1994,** *36* (2), 327-359.

[88] Rad, H. R. B.; Idris, M. H.; Kadir, M. R. A.; Farahany, S., Microstructure analysis and corrosion behavior of biodegradable Mg–Ca implant alloys. *Materials & Design* **2012,** *33*, 88-97.

[89] Salahshoor, M.; Guo, Y., Biodegradable Orthopedic Magnesium-Calcium (MgCa) Alloys, Processing, and Corrosion Performance. *Materials* **2012,** *5* (1), 135-155.

[90] Liu, C. L.; Wang, Y. J.; Zeng, R. C.; Zhang, X. M.; Huang, W. J.; Chu, P. K., In vitro corrosion degradation behaviour of Mg–Ca alloy in the presence of albumin. *Corrosion Science* **2010,** *52* (10), 3341-3347.

[91] Liu, X.-b.; Shan, D.-y.; Song, Y.-w.; Han, E.-h., Effects of heat treatment on corrosion behaviors of Mg-3Zn magnesium alloy. *Transactions of Nonferrous Metals Society of China* **2010,** *20* (7), 1345-1350.

[92] Larionova, T. V.; Park, W.-W.; You, B.-S., A ternary phase observed in rapidly solidified Mg–Ca–Zn alloys. *Scripta Materialia* **2001,** *45* (1), 7-12.

[93] Thekkepat, K.; Han, H.-S.; Choi, J.-W.; Lee, S.-C.; Yoon, E. S.; Li, G.; Seok, H.-K.; Kim, Y.-C.; Kim, J.-H.; Cha, P.-R., Computational design of Mg alloys with minimal galvanic corrosion. *Journal of Magnesium and Alloys* **2022,** *10* (7), 1972-1980.

[94] Nam, N. D., Role of Zinc in Enhancing the Corrosion Resistance of Mg-5Ca Alloys. *Journal of The Electrochemical Society* **2015,** *163* (3), C76-C84.

[95] Zhang, S.; Zhang, X.; Zhao, C.; Li, J.; Song, Y.; Xie, C.; Tao, H.; Zhang, Y.; He, Y.; Jiang, Y.; Bian, Y., Research on an Mg-Zn alloy as a degradable biomaterial. *Acta biomaterialia* **2010,** *6* (2), 626-40.

[96] Wang, H.; Song, Y.; Yu, J.; Shan, D.; Han, H., Characterization of Filiform Corrosion of Mg–3Zn Mg Alloy. *Journal of The Electrochemical Society* **2017,** *164* (9), C574-C580.

[97] Williams, G.; Birbilis, N.; McMurray, H. N., The source of hydrogen evolved from a magnesium anode. *Electrochemistry Communications* **2013,** *36*, 1-5.

[98] Cao, F.; Xiao, B.; Wang, Z.; Ying, T.; Zheng, D.; Atrens, A.; Song, G.-L., A Mg alloy with no hydrogen evolution during dissolution. *Journal of Magnesium and Alloys* **2021**.

[99] Thomas, S.; Medhekar, N. V.; Frankel, G. S.; Birbilis, N., Corrosion mechanism and hydrogen evolution on Mg. *Current Opinion in Solid State and Materials Science* **2015,** *19* (2), 85-94.

[100] Bender, S.; Goellner, J.; Heyn, A.; Schmigalla, S., A new theory for the negative difference effect in magnesium corrosion. *Materials and Corrosion* **2012,** *63* (8), 707-712.

[101] Bakhsheshi-Rad, H. R.; Hamzah, E.; Fereidouni-Lotfabadi, A.; Daroonparvar, M.; Yajid, M. A. M.; Mezbahul-Islam, M.; Kasiri-Asgarani, M.; Medraj, M., Microstructure and bio-

corrosion behavior of Mg–Zn and Mg–Zn–Ca alloys for biomedical applications. *Materials and Corrosion* **2014,** *65* (12), 1178-1187.

[102] Yan, Y.; Cao, H.; Kang, Y.; Yu, K.; Xiao, T.; Luo, J.; Deng, Y.; Fang, H.; Xiong, H.; Dai, Y., Effects of Zn concentration and heat treatment on the microstructure, mechanical properties and corrosion behavior of as-extruded Mg-Zn alloys produced by powder metallurgy. *Journal of Alloys and Compounds* **2017,** *693*, 1277-1289.

[103] Ha, H.-Y.; Kang, J.-Y.; Yang, J.; Yim, C. D.; You, B. S., Limitations in the use of the potentiodynamic polarisation curves to investigate the effect of Zn on the corrosion behaviour of as-extruded Mg–Zn binary alloy. *Corrosion Science* **2013,** *75*, 426-433.

[104] Ijaz, M.; Zafar, M.; Islam, A.; Afsheen, S.; Iqbal, T., A Review on Antibacterial Properties of Biologically Synthesized Zinc Oxide Nanostructures. *Journal of Inorganic and Organometallic Polymers and Materials* **2020,** *30* (8), 2815-2826.

[105] Yi, G.; Li, X.; Yuan, Y.; Zhang, Y., Redox active Zn/ZnO duo generating superoxide (˙O2−) and H2O2 under all conditions for environmental sanitation. *Environmental Science: Nano* **2019,** *6* (1), 68-74.

[106] Mukherjee, I.; Cilamkoti, V.; Dutta, R. K., Sunlight-Driven Photocatalytic Degradation of Ciprofloxacin by Carbon Dots Embedded in ZnO Nanostructures. *ACS Applied Nano Materials* **2021,** *4* (8), 7686-7697.

[107] Ren, K.; Yu, J.; Tang, W., First-principles study of two-dimensional van der Waals heterostructure based on ZnO and Mg(OH)2: A potential photocatalyst for water splitting. *Physics Letters A* **2019,** *383* (29), 125916.

[108] Lin, H. Y.; Chou, Y. Y.; Cheng, C. L.; Chen, Y. F., Giant enhancement of band edge emission based on ZnO/TiO2 nanocomposites. *Opt. Express* **2007,** *15* (21), 13832-13837.

[109] Singh, J.; Kaur, S.; Kaur, G.; Basu, S.; Rawat, M., Biogenic ZnO nanoparticles: a study of blueshift of optical band gap and photocatalytic degradation of reactive yellow 186 dye under direct sunlight. *Green Processing and Synthesis* **2019,** *8* (1), 272-280.

[110] He, W.; Zhao, H.; Jia, H.; Yin, J.-J.; Zheng, Z., Determination of reactive oxygen species from ZnO micro-nano structures with shape-dependent photocatalytic activity. *Materials Research Bulletin* **2014,** *53*, 246-250.

[111] Wang, B.-J.; Li, X.-H.; Cai, X.-L.; Yu, W.-Y.; Zhang, L.-W.; Zhao, R.-Q.; Ke, S.-H., Blue Phosphorus/Mg(OH)2 van der Waals Heterostructures as Promising Visible-Light Photocatalysts for Water Splitting. *The Journal of Physical Chemistry C* **2018,** *122* (13), 7075-7080.

[112] Kaneti, Y.; Zhang, Z.; Yue, J.; Quadir, M.; Chuyang, C.; Jiang, X.; Yu, A., ESI for PCCP paper. 2014.

[113] Qu, G.; Fan, G.; Zhou, M.; Rong, X.; Li, T.; Zhang, R.; Sun, J.; Chen, D., Graphene-Modified ZnO Nanostructures for Low-Temperature NO 2 Sensing. *ACS Omega* **2019,** *4*, 4221-4232.

[114] Heakal, F.; Bakry, A., Corrosion Degradation of AXJ530 Magnesium Alloy in Simulated Pysiological Fluid and Its Mitigation by Fluoride and Chitosan Coatings for Osteosynthetic Applications. *International journal of electrochemical science* **2018,** *13*, 7724-7747.

[115] Naqvi, S. M. A., *Structural and optical properties of chromium doped zinc oxide nanoparticles synthesized by sol-gel method*. 2014.

[116] Bououdina, M.; Azzaza, S.; Ghomri, R.; Shaikh, M. N.; Dai, J. H.; Song, Y.; Song, W.; Cai, W.; Ghers, M., Structural and magnetic properties and DFT analysis of ZnO:(Al,Er) nanoparticles. *RSC Advances* **2017,** *7* (52), 32931-32941.

[117] Chen, H.; Ma, X.; Zhang, J.; Li, Q.; Liu, H.; Chen, Z.; Chu, G.; Chu, S., Avalanche solar blind photodetectors with high responsivity based on MgO/MgZnO heterostructures. *Opt. Mater. Express* **2018,** *8* (4), 785-793.

[118] Liu, Z.; Yin, Z.; Cox, C.; Bosman, M.; Qian, X.; Li, N.; Zhao, H.; Du, Y.; Li, J.; Nocera, D. G., Room temperature stable COx-free H2 production from methanol with magnesium oxide nanophotocatalysts. *Science Advances* **2016,** *2* (9), e1501425.

[119] Ichimura, M., Calculation of Band Offsets of Mg(OH)2-Based Heterostructures. *Electronic Materials* **2021,** *2* (3), 274-283.

[120] Prausnitz, M. R.; Langer, R., Transdermal drug delivery. *Nature Biotechnology* **2008,** *26* (11), 1261-1268.

[121] Raphael, A. P.; Crichton, M. L.; Falconer, R. J.; Meliga, S.; Chen, X.; Fernando, G. J. P.; Huang, H.; Kendall, M. A. F., Formulations for microprojection/microneedle vaccine delivery:

Structure, strength and release profiles. *Journal of Controlled Release* **2016,** *225*, 40-52.

[122] Park, Y.-H.; Ha, S. K.; Choi, I.; Kim, K. S.; Park, J.; Choi, N.; Kim, B.; Sung, J. H., Fabrication of degradable carboxymethyl cellulose (CMC) microneedle with laser writing and replica molding process for enhancement of transdermal drug delivery. *Biotechnology and Bioprocess Engineering* **2016,** *21* (1), 110-118.

[123] Indermun, S.; Luttge, R.; Choonara, Y. E.; Kumar, P.; du Toit, L. C.; Modi, G.; Pillay, V., Current advances in the fabrication of microneedles for transdermal delivery. *Journal of Controlled Release* **2014,** *185*, 130-138.

[124] Wiraja, C.; Zhu, Y.; Lio, D. C. S.; Yeo, D. C.; Xie, M.; Fang, W.; Li, Q.; Zheng, M.; Van Steensel, M.; Wang, L.; Fan, C.; Xu, C., Framework nucleic acids as programmable carrier for transdermal drug delivery. *Nature Communications* **2019,** *10* (1), 1147.

[125] Vinayakumar, K. B.; Kulkarni, P. G.; Nayak, M. M.; Dinesh, N. S.; Hegde, G. M.; Ramachandra, S. G.; Rajanna, K., A hollow stainless steel microneedle array to deliver insulin to a diabetic rat. *Journal of Micromechanics and Microengineering* **2016,** *26* (6), 065013.

[126] Barry, B. W., Novel mechanisms and devices to enable successful transdermal drug delivery. *European Journal of Pharmaceutical Sciences* **2001,** *14* (2), 101-114.

[127] Tanner, E. E. L.; Curreri, A. M.; Balkaran, J. P. R.; Selig-Wober, N. C.; Yang, A. B.; Kendig, C.; Fluhr, M. P.; Kim, N.; Mitragotri, S., Design Principles of Ionic Liquids for Transdermal Drug Delivery. *Advanced Materials* **2019,** *31* (27), 1901103.

[128] Krieger, K. J.; Bertollo, N.; Dangol, M.; Sheridan, J. T.; Lowery, M. M.; O'Cearbhaill, E. D., Simple and customizable method for fabrication of high-aspect ratio microneedle molds using low-cost 3D printing. *Microsystems & Nanoengineering* **2019,** *5* (1), 42.

[129] Jeong, W. Y.; Kwon, M.; Choi, H. E.; Kim, K. S., Recent advances in transdermal drug delivery systems: a review. *Biomaterials Research* **2021,** *25* (1), 24.

[130] Arora, A.; Prausnitz, M. R.; Mitragotri, S., Micro-scale devices for transdermal drug delivery. *International Journal of Pharmaceutics* **2008,** *364* (2), 227-236.

[131] Prausnitz, M. R.; Mitragotri, S.; Langer, R., Current status and future potential of transdermal drug delivery. *Nature Reviews Drug Discovery* **2004,** *3* (2), 115-124.

[132] Prausnitz, M. R., Microneedles for transdermal drug delivery. *Advanced Drug Delivery*

Reviews **2004,** *56* (5), 581-587.

[133] Kolli, C. S.; Xiao, J.; Parsons, D. L.; Babu, R. J., Microneedle assisted iontophoretic transdermal delivery of prochlorperazine edisylate. *Drug development and industrial pharmacy* **2012,** *38* (5), 571-6.

[134] Bai, Y.; Sachdeva, V.; Kim, H.; Friden, P. M.; Banga, A. K., Transdermal delivery of proteins using a combination of iontophoresis and microporation. *Ther Deliv* **2014,** *5* (5), 525-36.

[135] Kim, S.-J.; Shin, J.-H.; Noh, J.-Y.; Song, C.-S.; Kim, Y.-C., Development of the novel coating formulations for skin vaccination using stainless steel microneedle. *Drug Delivery and Translational Research* **2016,** *6* (5), 486-497.

[136] Singh, N. D.; Banga, A. K., Controlled delivery of ropinirole hydrochloride through skin using modulated iontophoresis and microneedles. *Journal of Drug Targeting* **2013,** *21* (4), 354-366.

[137] Miller, P. R.; Moorman, M.; Boehm, R. D.; Wolfley, S.; Chavez, V.; Baca, J. T.; Ashley, C.; Brener, I.; Narayan, R. J.; Polsky, R., Fabrication of Hollow Metal Microneedle Arrays Using a Molding and Electroplating Method. *MRS Advances* **2019,** *4* (24), 1417-1426.

[138] Tsuchiya, K.; Jinnin, S.; Yamamoto, H.; Uetsuji, Y.; Nakamachi, E., Design and development of a biocompatible painless microneedle by the ion sputtering deposition method. *Precision Engineering* **2010,** *34* (3), 461-466.

[139] Parker, E. R.; Rao, M. P.; Turner, K. L.; MacDonald, N. C. In *Bulk Titanium Microneedles with Embedded Microfluidic Networks for Transdermal Drug Delivery*, 19th IEEE International Conference on Micro Electro Mechanical Systems, 22-26 Jan. 2006; 2006; pp 498-501.

[140] Brooks, E. K.; Brooks, R. P.; Ehrensberger, M. T., Effects of simulated inflammation on the corrosion of 316L stainless steel. *Materials Science and Engineering: C* **2017,** *71*, 200-205.

[141] Yang, J.; Guo, J. L.; Mikos, A. G.; He, C.; Cheng, G., Material Processing and Design of Biodegradable Metal Matrix Composites for Biomedical Applications. *Annals of Biomedical Engineering* **2018,** *46* (9), 1229-1240.

[142] Witte, F.; Feyerabend, F.; Maier, P.; Fischer, J.; Störmer, M.; Blawert, C.; Dietzel, W.;

Hort, N., Biodegradable magnesium–hydroxyapatite metal matrix composites. *Biomaterials* **2007,** *28* (13), 2163-2174.

[143] Pikal, M. J., The role of electroosmotic flow in transdermal iontophoresis. *Advanced Drug Delivery Reviews* **2001,** *46* (1), 281-305.

[144] Bernardi, D. S.; Bitencourt, C.; da Silveira, D. S. C.; da Cruz, E. L. C. M.; Pereira-da-Silva, M. A.; Faccioli, L. H.; Lopez, R. F. V., Effective transcutaneous immunization using a combination of iontophoresis and nanoparticles. *Nanomedicine: Nanotechnology, Biology and Medicine* **2016,** *12* (8), 2439-2448.

[145] Pradeep Narayanan, S.; Raghavan, S., Fabrication and characterization of gold-coated solid silicon microneedles with improved biocompatibility. *The International Journal of Advanced Manufacturing Technology* **2019,** *104* (9), 3327-3333.

[146] Li, J.; Liu, B.; Zhou, Y.; Chen, Z.; Jiang, L.; Yuan, W.; Liang, L., Fabrication of a Ti porous microneedle array by metal injection molding for transdermal drug delivery. *PLoS One* **2017,** *12* (2), e0172043.

[147] Zhang, W.; Liu, Q.; Chen, Y.; Wan, G., Anodic dissolution dictates the negative difference effect (NDE) of magnesium corrosion more in chemical pathway. *Materials Letters* **2018,** *232*, 54-57.

[148] Bok, M.; Lee, Y.; Park, D.; Shin, S.; Zhao, Z.-J.; Hwang, B.; Hwang, S. H.; Jeon, S. H.; Jung, J.-Y.; Park, S. H.; Nah, J.; Lim, E.; Jeong, J.-H., Microneedles integrated with a triboelectric nanogenerator: an electrically active drug delivery system. *Nanoscale* **2018,** *10* (28), 13502-13510.

[149] Bok, M.; Zhao, Z.-J.; Jeon, S.; Jeong, J.-H.; Lim, E., Ultrasonically and Iontophoretically Enhanced Drug-Delivery System Based on Dissolving Microneedle Patches. *Scientific Reports* **2020,** *10* (1), 2027.

[150] Ullah, A.; Kim, C. M.; Kim, G. M., Porous polymer coatings on metal microneedles for enhanced drug delivery. *Royal Society Open Science* **2018,** *5* (4), 171609.

[151] Garland, M. J.; Caffarel–Salvador, E.; Migalska, K.; Woolfson, A. D.; Donnelly, R. F., Dissolving polymeric microneedle arrays for electrically assisted transdermal drug delivery. *Journal of Controlled Release* **2012,** *159* (1), 52-59.

[152] Burnette, R. R.; Ongpipattanakul, B., Characterization of the Pore Transport Properties and Tissue Alteration of Excised Human Skin during Iontophoresis. *Journal of Pharmaceutical Sciences* **1988,** *77* (2), 132-137.

[153] Kumar, V.; Banga, A. K., Modulated iontophoretic delivery of small and large molecules through microchannels. *Int J Pharm* **2012,** *434* (1-2), 106-14.

[154] Stagni, G.; Ali, M. E.; Weng, D., Pharmacokinetics of acyclovir in rabbit skin after IV-bolus, ointment, and iontophoretic administrations. *International Journal of Pharmaceutics* **2004,** *274* (1), 201-211.

[155] Sznitowska, M.; Janicki, S., [Percutaneous absorption of heparin: a critical review of experimental results]. *Pol Merkur Lekarski* **2000,** *7* (43), 58-63.

[156] Lim, J.; Hoffmann, M. R., Substrate oxidation enhances the electrochemical production of hydrogen peroxide. *Chemical Engineering Journal* **2019,** *374*, 958-964.

국문 초록

마그네슘 (Mg)은 뛰어난 기계적 성질, 생체적합성, 그리고 생분해성의 특성으로 정형외과, 치과 등 다양한 의공학분야에서 사용되고 있다. 이러한 장점에도 불구하고 마그네슘 사용이 제한적인 이유는 활발한 부식 속도이다. 특히, 초기 부식 단계의 동적인 부식 거동은 세포 부착 및 세포-표면 결합에 결정적인 역할을 하며, 임플란트 재료의 성공 여부를 결정한다. 따라서 마그네슘의 부식 메커니즘을 이해하는 것이 매우 중요하다. 마그네슘과 그 합금은 부식 과정에서 수소기체 (H_2), 반응성산소종 (ROS) 및 다양한 산화물과 같은 부식 생성물을 생성한다. 이 논문에서 우리는 마그네슘과 그 합금의 부식 메커니즘에 대한 이해를 통해 부식 생성물을 제어하고 의공학분야에서의 활용을 확대하고자 하였다.

스텐트 기술의 혁신적인 발전에도 불구하고 재협착증은 스텐트의 임상 이식에 중요한 문제이다. ROS는 내피 세포(EC)와 평활근 세포(SMC)를 선택적으로 제어함으로써 잠재적으로 재내피화를 가속화하고 재협착의 방지하는 것으로 알려져 있다. 인체에서 ROS를 생성시키기 위해서는 초음파와 빛과 같은 다양한 외부자극이 필요하지만 갈바닉 부식은 간단한 코팅층만으로 ROS 생성을 쉽게 유도할 수 있다. 재내피화를 강화하고 재협착을 억제하기 위해 생분해성 폴리머와 이중 양극/음극 금속층으로 구성된 새로운 생분해성 하이브리드 재료를 보고한다. 순수 아연 (Zn) 및 Mg 박막을 DC 마그네트론 스퍼터링에 의해 Poly-l-lactic acid (PLLA) 기판에 증착하고, 생분해성 하이브리드 재료를 사용한 장기 침지 테스트를 인산염 완충 용액(PBS)에서 수행했다. 초과산화물 음이온과 과산화수소 모두 양극인 Mg 층이 완전히 소비된 후에도 원활하게 생성되었다. 따라서 PLLA 기반 하이브리드 소재의 부식에 의한 ROS 생성은 양극 금속층이 고갈될 때까지 지속될 수 있다.

둘째, 금속의 부식률은 대부분 수소기체의 발생으로 해석되었다. 그러나 의공학분야에서 ROS는 뛰어난 항균 작용과 암 치료 분야에서 활발히 연구되고 있다. 이에 따라 금속학적 요인을 기반으로 마그네슘 계 합금의 부식에 의한 ROS 발생의 가장 두드러진 요인을 찾고자 하였다. Mg 합금을 PBS용액에 침지하여 발생하는 ROS의 양을 측정하여, 부식에 의한 전자공급보다는 표면성질이 ROS생성에 더 중요하게 적용되었다. 그

증명실험으로 인위적으로 음극전류를 인가하여 자연부식의 영향을 최소화한 환경에서의 표면반응을 철저히 조사하였다. 그 결과 전자의 공급이 항상 ROS 생성에 관여하는 것은 아니었다. 또다른 증명실험인 산화막 그리고 ZnO 모델 테스트는 ROS의 생성에 있어 음극상의 종류와 표면에 형성된 산화막, 즉 합금 표면의 고유 특성이 ROS 발생에 가장 중요한 요인임을 분명히 입증하였다. 이를 통해 표면의 미세구조와 상 분석을 바탕으로 합금의 우세한 반응 예측이 가능할 뿐 아니라, 합금의 제조, 표면 코팅, 표면 처리 등으로 ROS 생성을 새롭게 유도할 수 있을 것이라 기대된다.

셋째, 생분해성 금속을 미세 바늘(MN)과 이온 영동을 적용하여 효과적인 경피약물전달을 위한 후보자로 철저히 연구되었다. 여기서 우리는 MN 전극의 두드러진 후보로 마그네슘을 제시한다. 금속 특성은 전압을 인가하여 하전된 약물 분자의 확산을 향상시킬 수 있는 반면, 과도한 전압인가는 과도한 수소기체를 발생시켜 약물 이동을 방해한다. 나노초 레이저를 이용하여 Mg MN 전극을 제작하였고, 이온영동시 인가된 전위로 수소기체의 양을 측정하였다. 따라서, 인가된 전위에 의한 향상된 약물 확산과 수소 발생으로 인한 방해의 결합된 효과에 기초하여 이온영동을 위한 적절한 전압인가가능 범위를 확립하였다. 돼지 피부에 대한 Mg MN의 염료 투과 시험은 Mg MN과 이온 영동의 결합된 효과를 입증했다. 과도한 수소 발생과 바늘 끝의 부식으로 인해 더 높은 전압에서 염료 이동이 감소했으며, 두 가지 모두 Mg MN 표면을 따라 하전된 염료 분자의 확산을 더 어렵게 만든다. 이러한 결과는 전압인가 동안 전기장 및 기포 생성을 통한 경피약물전달을 위한 Mg MN 전극의 최적의 잠재적 범위를 입증한다.

이로써 마그네슘과 마그네슘 합금의 갈바닉 부식, 마이크로 갈바닉 부식, 전기화학적 부식을 분석하고 부식생성물들을 이용하여, 스텐트 재협착 방지, 약물전달 등 다양한 의공학분야에 응용가능성을 확인하였다. 향후, 위의 연구결과들을 토대로, 생분해성 금속인 마그네슘의 활용 범위가 더울 넓어질 뿐 아니라, 부식 생성물의 발생을 적절히 제어하여 다양한 분야에서 효과적으로 적용될 수 있을 것이라 예상된다.